 doi:10.20944/preprints202106.0667.v1

Article

Air Quality in the Italian Northwestern Alps during Year 2020: Assessment of the COVID-19 «Lockdown Effect» from Multi-Technique Observations and Models

Henri Diémoz [1,‡,*], Tiziana Magri [1,‡], Giordano Pession [1], Claudia Tarricone [1], Ivan Karl Friedrich Tombolato [1], Gabriele Fasano [1,2], and Manuela Zublena [1]

[1] Regional Environmental Protection Agency (ARPA) Valle d'Aosta, 11020 Saint-Christophe (AO), Italy
[2] Sapienza University of Rome, 00185 Rome, Italy
[*] Correspondence: h.diemoz@arpa.vda.it; Tel.: +39-165-278576 (H.D.)
[‡] These authors contributed equally to this work.

Abstract: The effect of COVID-19 confinement regulations on air quality in the northwestern Alps is here assessed based on measurements at five valley sites in different environmental contexts. Surface concentrations of nitrogen oxides, ozone, particle matter, together with size, chemical, and optical (light absorption) aerosol properties, complemented by observations along the vertical column are considered. The 2020 concentration anomalies relative to previous years' average are compared with the output of a machine learning algorithm accounting for weather effects and a chemical transport model, their difference being within 10–20 %. Even in the relatively pristine environment of the Alps, the «lockdown effect» is well discernible, both in the early confinement phase and in late 2020, especially in NO_x concentrations (NO decreasing by $>$ 80 % and NO_2 by $>$ 50 %). While ozone shows little variation, secondary aerosols increase due to enhanced transport from the neighbouring Po basin and coarse particles decrease due to missing resuspension by traffic and, in the city, to the shutdown of a steel mill. The NO_2 vertical column density decreases by $>$ 20 %, whereas the aerosol profile is mainly influenced by large-scale dynamics, except a shallow layer about 500 m thick possibly sensitive to curtailed surface emissions.

Keywords: COVID-19; air quality; nitrogen oxides; ozone; aerosol; source apportionment; aerosol profiles; models; Alps; Italy

1. Introduction

Recent research highlights that the SARS-CoV-2 virus has already been circulating in Italy since December or even November 2019 [1,2], i.e. well before the first official detection in February 2020, and in different geographic areas simultaneously. In the absence of any containment measure, Italy – and notably its northern regions – became the European hotspot of the "first wave" of the COVID-19 pandemic. To curb the spread of the infection, distancing rules and restrictions to the circulation (lockdown regulations) were issued by the national government at the end of February 2020 and persisted, in varying degrees, throughout years 2020 and 2021. As a consequence, and as also occurred around the world, this has led to a sudden and countrywide shift in habits, energy consumption patterns and emissions in the atmosphere, thus representing an accidental, and hopefully unique, switch-off experiment of specific air pollution sources.

Similarly to other countries [e.g., 3–15], the «lockdown effect» on air quality in Italy has been observed and profusely studied, with special regard to the urban areas in the northern regions. Indeed, these latter were not only the first to introduce the new regulations and interrupt their business-as-usual activities, but they are also the most densely populated and industrialised, and – due to the orographical conformation of the Alps and the Apennines enclosing the Po basin and limiting ventilation – one of the European areas mostly impacted by atmospheric pollution. Several analysis techniques

 doi:10.20944/preprints202106.0667.v1

were adopted in different studies to assess changes in gas and aerosol concentrations measured in northern Italy, from both the ground and space, during the confinement phases with reference to a business-as-usual scenario, e.g. comparison to previous years, use of chemical transport models (CTMs) or statistical models (e.g., machine learning methods) trained on past data. A significant reduction of air pollutants due to vehicular circulation was found, as expected from the remarkable traffic abatement (e.g., reaching -71 % in Milan [16] and even larger decreases in other locations). Hence, for example, benzene and nitrogen oxides (NO_x) showed the largest reduction, with the former decreasing by 30–65 % [17–19], nitric oxide (NO) by 50–80 % [17–22] and nitrogen dioxide (NO_2) by 30–60 % [17–20,22,23], depending on the considered measurement station (environment) and the examined period [24]. Shutdown of industrial activities likely further contributed to the observed NO_x decline, e.g. in some northern provinces [16]. Changes were less pronounced for particle matter (PM) concentrations, with average reductions < 30 % for particles with aerodynamic diameter of 10 µm or less (PM_{10}) [18–20], and even lower for particles with aerodynamic diameter of 2.5 µm or less ($PM_{2.5}$) [23]. Peak PM concentrations, however, were observed to significantly decrease [18,19]. The limited changes in average PM concentrations, compared to the reductions in nitrogen oxides, were attributed to the heterogeneous, and more complex, nature of the aerosol particles, and notably to increase in domestic heating and wood combustion, based on measurements of larger light absorption Ångström exponents (AÅE), as well as enhanced secondary production [25,26]. No decreases were found for ammonia (NH_3), owing to the fact that emissions from the agricultural sector persisted during the lockdown period [18,19,22,27]. On the other hand, the increased concentrations of surface ozone (O_3), up to ca. 30 % in urbanised areas in April–May, were attributed to non-linear chemical effects [28] resulting from lower titration by NO and higher VOC-NO_x ratio [17,21,25]. Overall, the impact of the COVID-19 contingency measures in northern Italy was beneficial for the environment, by also reducing the carbon footprint [29], and for human health, partially compensating the years of life lost and the premature deaths attributable to COVID-19 during the same period [23]. Broadening the perspective to the whole country, all studies based on observations of surface concentrations both in single cities [30–33] and at multiple sites [34–36], and even on retrievals of columnar quantities [37,38], come to similar conclusions as those discussed above. Several of them additionally stress the importance of considering medium- and long-range transport of both anthropogenic and natural compounds during the examined period [31,35,37,38].

The vast majority of the published research focuses on very polluted areas, such as large conurbations and densely populated regions, where changes are more evident. To the best of our knowledge, very few studies address the effects of the COVID-19 confinement measures on air quality at more pristine, mountain sites [e.g., 39] or differentiate their outcomes based on landscape [40]. Additionally, most of the scientific literature available until now only covers the first half of year 2020, hence neglecting possible impacts on air quality during the following "waves" of the pandemic. In this regard, it is worth noting that, in mountainous regions, winter tourism normally brings an important increase in the traffic flux, e.g. towards ski resorts, which was instead almost absent during winter 2020–2021. The present paper tries to fill these gaps by considering air pollution data collected all-year-round (2020) in the Aosta Valley, a mountainous region in the European Alps. Indeed, air quality monitoring in this environment is particularly interesting owing to the peculiar meteorology (Sect. 2.1), which can enhance atmospheric pollutant concentrations at the surface even in the absence of strong emission sources [41]. Among these latter, for example, domestic wood burning is widespread and explains a large part of the carbonaceous aerosol emissions in the Alps [42,43]. Likewise, complex terrain can trigger local circulation regimes contributing to air pollutant removal or, conversely, to transport from the adjacent polluted forelands [44,45]. Once emitted into the Alpine atmosphere, air pollutants are not only harmful for human health, but they elicit direct and indirect radiative effects,

 doi:10.20944/preprints202106.0667.v1

particularly important at mountainous sites [46], and enter the water cycle through deposition on snow fields and glaciers [47].

Therefore, in the present study, we aim at answering the following, and still not fully explored, research questions:

- Q1: are changes to atmospheric composition limited to strongly polluted regions, or do they extend to remote and relatively pristine areas as well, such as the Alps?
- Q2: what is the magnitude, and even the sign (due to complex and non-linear effects), of the variations of surface air pollutant concentrations in the Alps during the confinement periods? Are these effects constant throughout 2020 or do they change in the distinct phases of the control measures?
- Q3: what source profiles can be identified in the Alps? Which of them actually change during the COVID-19 lockdown and which ones remain stable?
- Q4: what is the agreement among the estimates of the «lockdown effect» from different methods? How accurate are the existing CTMs and their emission inventories, and notably their modifications during the pandemic?
- Q5: how large is the influence of Alpine meteorology in 2020 compared to the effect of curtailed emissions?

These questions are here addressed by considering surface measurements of the most commonly monitored air pollutants (gases and PM) at five stations located in the Aosta Valley at short spatial distance ($<$ 70 km) in different types of environments (traffic, urban background, industrial, semi-rural, and rural), and by using different methodologies, such as comparison with average values from previous years, statistical models including weather normalisation, CTMs, and source apportionment techniques based on aerosol chemical composition, size, and optical properties. Moreover, aerosol vertical profiles and column-integrated quantities (NO_2 vertical column density and aerosol optical depth) are analysed to support and complement the measurements at the surface.

The paper is organised as follows: the investigated area and the data used in the study are described in Sect. 2 and the different methods employed to evaluate the impact of COVID-19 restrictions are introduced in Sect. 3. The main outcomes are presented and commented in Sect. 4. Finally, conclusions are drawn in Sect. 5.

2. Data

In this section, we introduce the domain of the study (Sect. 2.1), the sites and the instruments (Sect. 2.2) used to measure the most commonly monitored atmospheric pollutants. We also briefly describe the main confinement regulations adopted by the national and regional governments to reduce the transmission of SARS-CoV-2, which mark the distinct periods analysed here (Sect. 2.3).

2.1. Investigated area and sampling sites

The area investigated in the present study is the Aosta Valley (Fig. 1), a 80$\times$40 km^2 Italian region inhabited by ca. 126000 residents. It is located in the northwestern European Alps, its entrance, on the southeastern side, opening onto the Po basin and the other end overlooking the Mont Blanc massif, one of the highest chains in continental Europe (top altitude 4810 m a.s.l.). Several tributary valleys, hosting small villages, branch off the main valley, surrounded by mountain ridges as high as 4000 m a.s.l. Thus, not surprisingly, the average altitude of the region is higher than 2000 m a.s.l., and a wide portion of the terrain is covered with snow for a large part of the year.

The complex orography triggers some meteorological phenomena typical of mountain valleys. For instance, temperature inversions and cold-pool events, favouring the accumulation of air pollutants at the bottom of the valley, occur frequently, especially in winter. Thermally driven, up-valley and up-slope winds develop during fair-weather days (down-valley and down-slope winds during the night). A notable example of this circulation are easterly winds, which often carry atmospheric pollution and moisture

Preprints (www.preprints.org) | NOT PEER-REVIEWED | Posted: 28 June 2021 doi:10.20944/preprints202106.0667.v1

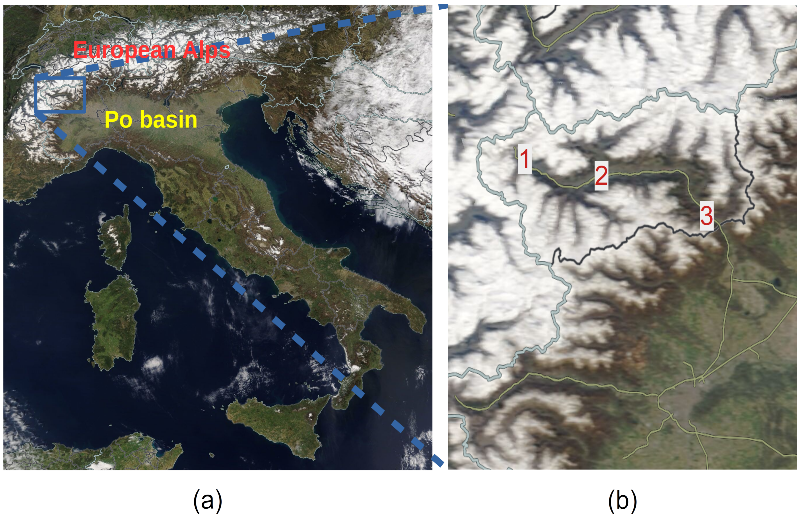

Figure 1. (**a**) Italy and (**b**) the Aosta Valley as seen from space by the MODIS radiometer (source: https://worldview.earthdata.nasa.gov/, image from 30 March 2021). The Alps and the Po basin are highlighted in the left panel, while the locations considered in the study are shown in the right panel: Courmayeur (1), Aosta (2), and Donnas (3).

from the Po basin to the valley [44,45,48]. Conversely, westerly winds (some of them, warm Foehn winds) contribute to clean up the air and improve the air quality.

The most relevant air pollutant sources within the region are domestic heating (some of it being from wood, especially in rural areas) and light and heavy vehicular traffic along the main route (central valley and cross-border traffic). Industry and agriculture/farming represent minor sectors and weaker contributors to atmospheric pollution. Finally, given its geographical position in-between the Mediterranean basin and continental Europe, the region is not uncommonly affected by transport of mineral dust from the Sahara desert.

The air quality network (Sect. 2.2) of the local regional environment protection agency (ARPA) mainly develops along the main valley. Five sites, representative of different environmental conditions, are chosen here (Fig. 1b and Table 1). The station of Courmayeur (1325 m a.s.l.) is located close to the road to the Mont Blanc tunnel, an international hub to France and an important artery between southern and continental Europe. Hence, Courmayeur represents a traffic station, despite the overall context being otherwise rural. Aosta (580 m a.s.l.) is the main settlement of the valley and its regional capital, hosting 34000 inhabitants. The Aosta–downtown station is located in a residential and commercial area in the heart of the city, and is partly influenced by a large steel mill operating at the southern border of the built-up area, which is the main source of trace metal elements in the local atmospheric aerosols. For this reason, an air quality sampling site is operated close to the mill, about 520 m south of Aosta–downtown. Given the very specific nature of this monitoring station, Aosta–industrial is only used in this study to assess the changes in PM loads during the closing period of the factory (Sect. 2.3). The downtown surface instrumentation (Sect. 2.2) is complemented by remote sensing instruments located at the ARPA solar observatory in Aosta–Saint-Christophe (560 m a.s.l., WIGOS ID 0-380-5-1), in a semi-rural area 2.5 km east of the city centre. Finally, Donnas (341 m a.s.l.) is a village in a rural context, at the border with the Po basin, and hence partly influenced by air pollution transport from the plain. The emissions in Donnas are linked to agricultural activities (e.g., burning of agricultural waste) and, only marginally, to highway traffic.

Overall, air pollutant concentrations in the Aosta Valley can be considered low, with yearly average NO concentrations of about 20 µg m^{-3} (much lower in Donnas, about 3 µg m^{-3}), 25 µg m^{-3} for NO_2 (<15 µg m^{-3}, in Donnas), 55 µg m^{-3} for O_3, 10 µg

Preprints (www.preprints.org) | NOT PEER-REVIEWED | Posted: 28 June 2021 doi:10.20944/preprints202106.0667.v1

Table 1. Measurement stations and corresponding instrumentation employed in this study. The time span when the data from each specific instrument are available and the portion employed in the present research are also listed.

Station	Measured quantity	Instruments	Data availability (used)
Courmayeur	NO_x	API200E Teledyne	2004–now (2015–2020)
Rural traffic	$PM_{2.5}$ and PM_{10} hourly concentration	Fidas200E Palas	2018–now[a] (2018–2020)
1325 m a.s.l.	and size distribution		
45.82N, 6.96E	PM_{10} hourly concentration	TEOM1400A	2007–2018 (2015–2018)
	Standard meteorological variables	Various	2007–now (2015–2020)
Aosta–downtown	NO_x	APNA370 Horiba	2010–now (2015–2020)
Urban background	O_3	API400E Teledyne	2004–now (2015–2020)
580 m a.s.l	$PM_{2.5}$ and PM_{10} daily concentration	SM200 Opsis	2012–now[b] (2015–2020)
45.73N, 7.32E	$PM_{2.5}$ and PM_{10} hourly concentration	Fidas200E Palas	September 2019–now (2020)
	and size distribution		
	Water-soluble anion-cation daily concentration	Dionex ion chromatography system	2017–now (2017–2020)
	EC/OC on PM_{10} samples	Sunset thermo-optical analyser	2017–now[c] (2017–2020)
	Levoglucosan on PM_{10} samples	Trace1300 Thermo Scientific	2018–now[c] (2018–2020)
	Metals on PM_{10} samples	Varian820-MS	2000–now[d] (2015–2020)
	Light absorption by particles	Aethalometer AE33 Magee Sci.	2020–now (2020)
	Standard meteorological variables	Various	1995–now (2015–2020)
Aosta–industrial	NO_x	APNA370 Horiba	2018–now (not used here)
Industrial	PM_{10} daily concentration	SM200 Opsis	2012–now (not used here)
570 m a.s.l	$PM_{2.5}$ and PM_{10} hourly concentration	Fidas200E Palas	2019–now (2019–2020)
45.73N, 7.32E	and size distribution		
	Metals on PM_{10} samples	Varian820-MS	2012–now (2015–2020)
Aosta–Saint-Christophe	NO_2 VCD	MkIV Brewer	2007–now[e] (2015–2020)
Semi-rural	Column aerosol properties	POM-02 Prede	2012–now[f] (2015–2020)
560 m a.s.l	Aerosol vertical profile	CHM15k-Nimbus Lufft	April 2015–now (2016–2020)
45.74N, 7.35E	$PM_{2.5}$ and PM_{10} hourly concentration	Fidas200E Palas	June 2017–February 2019
	and size distribution		(June 2017–February 2019)
Donnas	NO_x	API200E Teledyne	2006–now (2015–2020)
Rural background	O_3	API400E Teledyne	1995–now (2015–2020)
341 m a.s.l.	PM_{10} daily concentration	SM200 Opsis	2011–now (2015–2020)
45.60N, 7.77E	Standard meteorological variables	Various	1996–now (2015–2020)

[a] In Courmayeur, only PM_{10} measurements from the Fidas200E and the TEOM1400A are analysed in this study, since the $PM_{2.5}$ series is too short. [b] $PM_{2.5}$ only until end of 2019. [c] The analysis is performed on 4 out of 10 days according to the laboratory schedule, except for 2020, when analyses are performed along with the metal and anion/cation characterisation (on 6 out of 10 days). [d] The analysis is performed on 6 out of 10 days according to the laboratory schedule. [e] No NO_2 VCDs available for 2016. [f] Underwent major maintenance in the second half of 2016 and January 2017.

m^{-3} for $PM_{2.5}$ (5 µg m^{-3}, in Courmayeur), and <20 µg m^{-3} for PM_{10} (10 µg m^{-3}, in Courmayeur).

2.2. Experimental setup

In-situ surface measurements of common atmospheric pollutants are routinely carried out in the frame of the activities of the regional air quality network (Table 1). NO_x are monitored with hourly frequency using API200E (Teledyne) and APNA370 (Horiba) chemiluminescence analysers in Courmayeur, Aosta–downtown, Aosta–industrial, and Donnas, while O_3 is measured only in Aosta–downtown and Donnas by means of API400E (Teledyne) UV absorption analysers. Daily averages of $PM_{2.5}$ (2.3 m^3 h^{-1} sampling fluxes) were collected until 2019 by SM200 (Opsis) beta-attenuation particulate monitors in Aosta–downtown, and PM_{10} (1 m^3 h^{-1}) concentrations are collected in Aosta–downtown, Aosta–industrial, and Donnas with similar instruments. Tapered element oscillating microbalance (TEOM1400a) monitors [49] were used until the last few years to measure PM hourly concentrations at the air quality stations and were progressively replaced by new generation instruments. TEOM instruments do not compensate for mass loss of semi-volatile compounds [45,50], which might introduce systematic errors, e.g. in presence of an abundant fraction of secondary aerosols [51]. For this reason,

Preprints (www.preprints.org) | NOT PEER-REVIEWED | Posted: 28 June 2021 doi:10.20944/preprints202106.0667.v1

PM concentrations are also retrieved in Courmayeur (since 2018), Aosta–downtown (since September 2019), Aosta–industrial (since 2019), and Aosta–Saint-Christophe (June 2017–February 2019) with Fidas200E (Palas) aerosol spectrometers. These instruments provide simultaneous measurement of $PM_{2.5}$ and PM_{10} fractions for regulatory air pollution control according to the EN 16450, and volume and mass distributions, split in 64 classes, of particles sized between 0.18 and 18 µm. For the whole network, the QA/QC controls required by European technical standards are applied in compliance with the requirements of the air quality directive (2008/50/EC and 2004/107/EC).

Furthermore, PM_{10} aerosol samples are characterised for their chemical composition in Aosta–downtown and, for metals only, in Aosta–industrial. At the former station, samples collected by the SM200 on PTFE-coated glass fiber filters are analysed in the laboratory using a Dionex ion chromatography system (AQUION/ICS-1000 modules), allowing us to determine the mass concentrations of Cl^-, NO_3^-, SO_4^{2-}, Na^+, NH_4^+, K^+, Mg^{2+}, and Ca^{2+} water-soluble ions. Conversely, samples collected on quartz fibre filters by a co-located MCZ Micro-PNS type LVS16 low volume sequential particulate sampler (10 µm cutoff diameter, 2.3 $m^3\ h^{-1}$) are analysed alternatively for elemental/organic carbon (EC/OC, using a thermo-optical transmission method on portions of 1 cm^2 punches and following the EUSAAR-2 protocol [52]) and for metals (Cr, Cu, Fe, Mn, Ni, Pb, Zn, As, Cd, Mo, and Co, by means of inductively coupled plasma mass spectrometry after acid mineralisation of the filter in aqueous solution). Together with EC/OC, we also assess the concentration of levoglucosan, an organic compound belonging to the anhydrous sugar family and a tracer of fresh biomass combustion emissions in the atmosphere, through chemical treatment and analytical determination using gas-chromatography with flame ionization detector (GC-FID), after acetonitrile solid-liquid extraction. Finally, a dual-spot AE33 aethalometer [53] is employed in Aosta–downtown to characterise aerosol particles for their spectral light absorption properties at seven wavelengths in the UV, visible, and near infrared range (370–950 nm), and to determine the equivalent black carbon (eBC) concentrations at the surface and its source apportionment (Sect. 3.4.2). The dual-spot technology allows to compensate for the loading effect [53], while the scattering effect is corrected (with a coefficient $C = 1.57$). The aethalometer is operated at 0.3 $m^3\ h^{-1}$ total flow and 1 min time resolution.

As column-integrated quantities and vertical profiles are also important to understand the atmospheric dispersion dynamics and to identify transport from distant sources, remote sensing instrumentation is operated at Aosta–Saint-Christophe. A MkIV Brewer is used to retrieve NO_2 vertical column densities (VCDs) from direct-sun measurements of visible light at six wavelengths in the 425–453 nm range, with a recently developed algorithm [54,55]. A POM-02 (Prede) sun/sky radiometer detects solar radiation coming from the sun or scattered from the sky at different angles, which enables the retrieval of aerosol optical depth and properties in the column [46,56] by means of the Sunrad [57] and Skyrad MRI2 [58] inversion codes (here we exclusively use the former since only aerosol optical depths are investigated). The radiometer is calibrated on site with the "improved Langley method" [59], which is commonly employed in the SKYNET network. Finally, vertical profiles of particle backscatter (and derived products [60]) are obtained from a CHM15k-Nimbus (Lufft) automated lidar ceilometer (ALC), following the procedure described in previous publications [44,45]. The ALC calibration factor is determined at every clear-sky night using the Fernald-Klett method ("Rayleigh calibration") [61,62]. The results are carefully checked, the outliers are removed, and the calibration factors passing the selection criteria are interpolated using a local polynomial regression (LOESS) to account for seasonal changes in the ALC sensitivity. The correction for the partial overlap in the layers close to the surface is performed using the overlap function provided by the manufacturer, further corrected for changes of the internal instrumental temperature [63]. The particle backscatter is finally calculated with a forward method [64].

 doi:10.20944/preprints202106.0667.v1

Table 2. Definition of the periods employed in this study based on the different lockdown phases. The initials of the months are reported in the short name for ease of understanding.

Short name	Key dates (dd/mm/yyyy)	COVID-19 restrictions
P1(JFM)	01/01/2020 – 08/03/2020	Pre-lockdown, business-as-usual phase
P2(MA)	09/03/2020 – 13/04/2020	Strict lockdown, stay-at-home policy and steel mill closed
P3(AM)	14/04/2020 – 04/05/2020	Confinement measures continue, steel mill reopens
P4(MJ)	05/05/2020 – 03/06/2020	Progressive lockdown easing, justified movements within the region allowed
P5(JJASO)	04/06/2020 – 31/10/2020	Further relaxation, travels between regions allowed, schools open in September
P6(ND)	01/11/2020 – 31/12/2020	Schools partially close, ban on travels between regions

All stations are equipped with instruments providing standard meteorological variables, such as temperature, pressure, relative humidity, precipitation, surface wind velocity, and solar irradiance. A Viacount II (Famas System) microwave traffic counter was furthermore installed in Aosta, just outside the city centre on a busy road representative of the urban car traffic. Several short-term campaigns, each lasting few days, were organised between April and December 2020 to assess the number of passing vehicles.

2.3. Definition of the lockdown phases based on regional and national regulations

The first SARS-CoV-2 outbreak was officially reported in some municipalities in northern Italy at the end of February 2020. Following this event, national and regional regulations were issued to contain the infections and pressure on hospital facilities. In particular, since 9 March, a rapid succession of decree-laws led to closure of schools, public spaces, offices, food services, retail business, and industrial activities, thus defining the beginning of the strict "lockdown" period. Obviously, this also impacted on all non-essential activities in the Aosta Valley. Among them, the steel mill in proximity of Aosta was completely closed until 14 April. In response to the infection decline, the so-called "phase 2", envisaging a progressive lifting of the containment measures, and allowing displacements within the regional territory, started at the beginning of May. Circulation on the national territory was again permitted since June. New restrictions, such as closures and the night curfew, proved to be unavoidable since November, owing to the second pandemic "wave", i.e. a second and rapid increase of the COVID-19 cases, and lasted the whole 2020–2021 winter. For a winter tourism destination such as the Aosta Valley, this meant the complete absence of the seasonal visitor flux and the related traffic. Based on the above sequence of events, we identify six periods representative of the lockdown phases and their resulting impact on air quality. These are shown in Table 2. Anomalies with respect to a business-as-usual reference are then assessed separately for each of the periods.

3. Methods

In order to assess the effects of the curtailed emissions on the measured air pollutant concentrations, a reference (counterfactual) 2020 scenario, representative of business-as-usual conditions, is required for comparison with conditions actually met during this year. The reference might be chosen among an average from previous years' measurements (Sect. 3.1), the results of an empirical forecast accounting for weather influence (Sect. 3.2) or a deterministic, chemical transport model (Sect. 3.3). The relative difference in the concentration of each air pollutant i during the period j (anomaly, D_{ij}) between the perturbed scenario ($C_{ij}^{lockdown}$) and the selected reference (C_{ij}^{ref}) is then calculated as

$$D_{ij} = \frac{C_{ij}^{lockdown} - C_{ij}^{ref}}{C_{ij}^{ref}} \cdot 100\% \tag{1}$$

Preprints (www.preprints.org) | NOT PEER-REVIEWED | Posted: 28 June 2021 doi:10.20944/preprints202106.0667.v1

Table 3. Air pollutants modelled with the random forest technique (output), for the three considered sites, and explanatory variables (input).

Site	Modelled air pollutants	Meteorological variables (same for all stations)	Temporal variables (same for all stations)
Courmayeur	NO, NO_2, PM_{10}	Air temperature, wind speed and direction, relative humidity, global solar radiation, atmospheric pressure, daily precipitation amount	Julian day, day of week, date (Unix timestamp)
Aosta–downtown	NO, NO_2, O_3, $PM_{2.5}$, PM_{10}		
Donnas	NO, NO_2, O_3, PM_{10}		

Furthermore, based on the detailed characterisation of particle size, composition and light absorption properties available in Aosta–downtown, we are able to apply additional advanced, multivariate analysis techniques to the aerosol data sets collected at this station (Sect.3.4).

3.1. Comparison to previous years' averages

A first and basic method to obtain a reference series (C_{ij}^{ref}) is to calculate the average, for each of the analysed periods, of the concentrations measured in the years prior to 2020, i.e. before the spread of the pandemic and the contingency regulations. The series must be sufficiently long, in order to be representative of average conditions and not much impacted by anomalous meteorological conditions. At the same time, the average period should be short enough to ignore any long-term trend present in the data set (or assume that the meteorological variability has a larger effect) and not to introduce a bias in the calculation of the 2020 anomaly [65]. An average over the last 5 years prior to 2020 is therefore believed to be a good compromise. Hence, the 2015–2019 period is used when a whole series is available for this span, otherwise a subset is chosen (Table 1). When an instrument is replaced with a new one, data from both data sets are merged to provide a long-term average, after carefully checking that they agree over the overlapping period. Comparison to previous years' averages is applied to both surface concentrations and quantities measured along the vertical profile. Owing to the reduced data set and the peculiar conditions of the Aosta–industrial site, the series collected there are only used, in the following, for specific investigations and are excluded from the statistical analysis and simulations.

3.2. Predictive statistical models (random forest)

A major drawback of the method described above is that the influence due to meteorology is not explicitly accounted for and not disentangled from changes due to emissions. To overcome this limitation, we adopt predictive statistical models based on machine learning techniques. These methods aim to assess the dependence of a measured concentration from a set of known quantities, called explanatory variables, which are assumed to be representative of local atmospheric processes impacting on air pollutant dispersion. In particular, the set of explanatory variables typically consists of meteorological factors (e.g., wind intensity and direction, air temperature, global solar radiation, pressure) and temporal variables, which are used as predictors of daily, weekly and seasonal cycles of pollutant emissions.

In this study, `rmweather`, an open-source implementation of the random forest algorithm in the `R` language [66–68], is employed for counterfactual modelling of air pollutant surface concentrations in Courmayeur, Aosta–downtown, and Donnas, based on a set of explanatory variables, listed in Table 3. The accuracy of the method is evaluated in the following way [69]. Several models are trained for validation purposes over five periods (of 5 years each), i.e. 2010–2014, 2011–2015, 2012–2016, 2013–2017, 2014–2018, and they are compared with real measurements from years 2015, 2016, 2017, 2018, and 2019, respectively. The metrics of the comparison are reported in the Supplementary

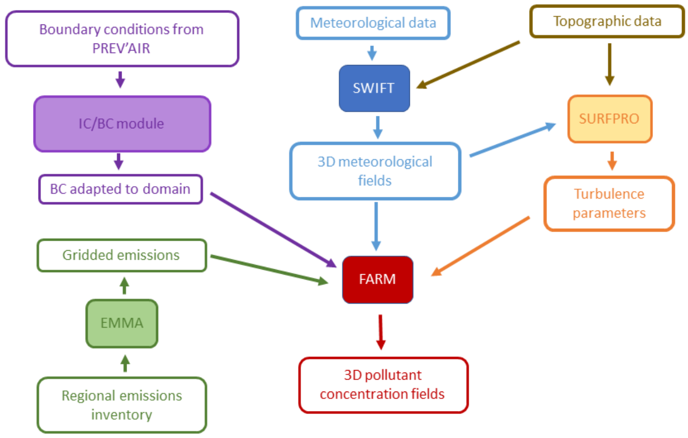

Figure 2. Summary of the components of the modelling chain used in this study.

Materials (Sect. S1) and show that the model performs well. Indeed, the Pearson's correlation indices between simulations and observations are almost always 0.9 for gases in Aosta–downtown and in Donnas (here with the exception of NO, likely more dependent on the instantaneous traffic fluxes or short-term weather effects), and the mean bias generally amounts to few $\mu g\ m^{-3}$. The complex meteorological and emission conditions in Courmayeur are more difficult to parameterise, however the Pearson's coefficients are still within 0.6 and 0.8. The random forests for PM_{10} perform slightly worse than gases, likely due to longer particle lifetime and a wider range of sources, but the correlation coefficient is anyway rather large (> 0.7 in most cases). Likewise, the predictive models for 2020 (Sect. 4.2–4.3), for each air pollutant and site, are trained over the period 2015–2019. This provides the required 2020 counterfactual scenario, accounting for specific weather effects.

3.3. Chemical transport model

The CTM chain used in this study is based on the flexible air quality regional model (FARM, http://www.farm-model.org, last access: 22 June 2021), a 3D Eulerian model accounting for transport, chemical conversion and deposition of atmospheric pollutants [e.g., 70–72]. The system relies on additional data provided by emission inventories (Sect. 3.3.1), considering both local (i.e., within the boundaries of the domain) and remote sources ("boundary conditions"), and by a meteorological model coupled with a tool for the estimation of the turbulence parameters (Sect. 3.3.2). A scheme of the simulation chain is provided in Fig. 2.

FARM (version 4.7) can process air pollutant emissions from both area and point sources, by considering transport and gas-phase chemical transformations according to the SAPRC-99 chemical scheme [73]. Primary and secondary particle dynamics, and their interactions with gas-phase species, are handled by the AERO3_NEW module, which includes nucleation, condensational growth, and coagulation processes [74]. Further details on the FARM working principles are provided elsewhere [e.g., 44,45].

In this study, the modelling system is run on a $110 \times 70\ km^2$ domain, roughly corresponding to the Aosta Valley (Fig. 1b), on a 1-km spatial grid and at 1-hour time steps. 16 different vertical levels (from the surface to 9290 m) are considered. Two runs relative to 2020 (each one over 366 days) are performed. The first simulation incorporates emissions from the previous year (2019, assuming no relevant variation compared to,

 doi:10.20944/preprints202106.0667.v1

e.g., 2015–2018) as reference scenario, while in the second one curtailed emissions are used, as explained in the next section (lockdown scenario). The same meteorological fields, from 2020 (Sect. 3.3.2), are kept in both runs.

3.3.1. Emissions and their modifications during the pandemic

The regional emission inventory of the Aosta Valley is fully set up and maintained in-house and is detailed according to the 11 conventional categories of the selected nomenclature for air pollution (SNAP97, Table S6 in the Supplementary Materials), depending on the local emission sources provided by the European coordination of information on the environment method (CORINAIR, https://www.eea.europa.eu/publications/EMEPCORINAIR5, last access: 22 June 2021). The inventory includes the estimated emissions of several atmospheric pollutants, such as NO_x, PM, NH_3, heavy metals, and of the most important greenhouse gases (CO_2, CH_4, N_2O).

These emission data are pre-processed by the emission manager (EMMA, http://doc.aria-net.it/EmissionManager, last access: 22 June 2021) and interpolated to every cell of the domain grid $\vec{x}$. The modulation of the mass emissions $E_i(\vec{x}, t)$ is described using a temporal profile for each air pollutant i, based on the number/power $A_j(\vec{x}, t)$ of the considered emitter j and a set of estimated emission factors F_{ij} (expressed as mass in relation to the activity index A), according to the following formula:

$$E_i(\vec{x}, t) = \sum_j A_j(\vec{x}, t) \cdot F_{ij} \tag{2}$$

The emission factors (for every type of source j and pollutant i) are generally those reported in the atmospheric emission inventory guidebook [75], unless more specific or up-to-date information is applicable based on the expertise of the operator and knowledge of the processes acting on a regional scale.

As anticipated, two distinct scenarios – a reference (2019) and a curtailed (2020) one – are used, with differences in emissions by the industrial and road transport sectors. The other sources, such as agriculture and waste, are left unchanged. Among them, domestic heating in 2020 is assumed to be not impacted by the restrictions. As instance, methane consumption from January to April (2019 and 2020) provided by the national methane pipeline society (SNAM) are compared, resulting in about the same values (yearly average difference < 1 %). Emissions from the steel mill in Aosta, which is the only relevant industrial establishment in the region, are modulated based on flume flows collected at the main chimney. This is particularly important from March to mid-April 2020 (period 2 in Table 2), when the industrial plant is closed due to the complete lockdown. Finally, variations in international and local road traffic are quantified based on vehicle flow measurements from several sources, such as data provided by the administration of the Mt. Blanc tunnel, specifically-designed webcams on motorway and regional roads, and traffic counters on urban roads (Sect. 2.2). Traffic reductions – reaching nearly 100 % through the Mt. Blanc tunnel in P2–P3, 90 % on the motorway, and 75–80 % on the other roads (notably, in the Aosta urban road network) – likely represent the most relevant effect of the confinement measures on emission abatement in the Aosta Valley, as also found by previous research in other regions.

The boundary conditions, used to estimate the air mass exchange from outside the borders of the FARM domain, are prepared starting from the daily simulations elaborated on a continental scale with the CHIMERE model [76] and operationally made available by the Prev'Air service (http://www.prevair.org, last access: 22 June 2021). Such boundary conditions, provided by the regional environmental protection agency of Piedmont for year 2020, are used as-is for both (lockdown and business-as-usual) emission scenarios, since they are not released separately for real and counterfactual conditions. Indeed, an accurate modulation of the national and continental emissions, and notably their anthropogenic fraction, would require an extremely large effort which is out of the scope of this work and would anyway result in considerable uncertainties

 doi:10.20944/preprints202106.0667.v1

(e.g., effect of regulations on secondary air pollutants). As a consequence, the observed changes in concentrations resulting from FARM simulations describe the effect from local emissions only.

3.3.2. Diagnostic meteorological model and turbulence pre-processor

SWIFT [77,78], a variational 3D wind model, is invoked to produce a mass consistent wind field over complex terrain at local and regional scale starting from wind measurements from a meteorological network (temperature and humidity fields can be interpolated, too). The model uses the first Navier-Stokes equation and the mass conservation to account for the effect of terrain on the flow structure. Here we use data every 30 minutes from 25 meteorological stations in the Aosta Valley. A turbulence and deposition pre-processor (surface-atmosphere interface processor, SURFPRO) computes the gridded fields of the planetary boundary layer turbulence scaling parameters, horizontal and vertical eddy diffusivities and deposition velocities according to land cover type, atmospheric circulation conditions and characteristics of the different chemical species [79].

3.4. Aerosol source apportionment

To accurately identify the particle emission sources and their evolution during 2020, we process the aerosol chemical and/or dimensional properties available at some of the sampling sites, using the positive matrix factorisation (PMF) technique (Sect. 3.4.1), and aerosol surface optical properties, taking advantage of the different spectral light absorption characteristics of fossil fuel and biomass burning components (Sect. 3.4.2).

3.4.1. Positive matrix factorisation

This technique [80,81] splits a multivariate series (e.g., a set of aerosol properties over time) into two matrices containing only non-negative elements, defining the strength and the characteristics of each source, respectively, in a similar way as already described in another context by Eq. 2. Keeping the same formulation as in Sect. 3.3.1,

$$C_i(t) = \sum_j A_j(t) \cdot F_{ij} \tag{3}$$

where $C_i(t)$ is, in this case, the mass concentration of element i at the receptor (either a chemical element or a size class, part of a multivariate data set), $A_j(t)$ is a measure of the activity of source j, and F_{ij} is the source profile, i.e. a description of the emission type with reference to the available elements sampled. The purpose of PMF is to identify sets of elements varying together (within the same group), thus attributed to the same source, while the contribution of each source is temporally uncorrelated to the other. The US EPA PMF5.0 implementation [82] is here employed to factorise both the dimensional data set from the three Fidas200E optical particle counters, and the Aosta–downtown chemical characterisation. In the first case, the variables are the 64 dimensional classes measured at hourly frequency (the results are then averaged at daily resolution). Compared to a subjective choice of the size classes, such as e.g. PM_1, $PM_{2.5}$ or PM_{10}, this "size-PMF" allows the different modes to arise naturally. In the second case ("chem-PMF"), the considered elements are the chemical elements listed in Sect. 2.2, originally collected at daily resolution. Since the whole chemical characterisation is not available at the same time owing to the used schedule (Table 1), three different combinations based on the simultaneous information, i.e. anion/cation only, anion/cation together with coincident organic carbon analyses, and anion/cation with metals are possible [45]. However, in order not to duplicate information, we only limit ourselves to analyse the last two data sets, i.e. the most complete ones. In particular, the series with levoglucosan and EC/OC (464 days) helps us to differentiate between biomass and non-biomass combustion processes, while the one with metals (856 days) allows us to assess the effect of the industrial lockdown on the air quality in Aosta–downtown. NO and NO_2

Preprints (www.preprints.org) | NOT PEER-REVIEWED | Posted: 28 June 2021 doi:10.20944/preprints202106.0667.v1

from co-located measurements are additionally included in chem-PMF to facilitate the identification of local air pollution sources. For both decompositions, the number of factors for each data set is chosen based on physical interpretability of the resulting factors and on the ratio of the goodness of the fit to its expected value (Q/Q_{exp}) [82]. The ratio should not exceed an empirical value of about 2, otherwise it is very likely that some samples and/or species are not well modelled and another source should be added. PM_{10} is considered as a total variable, i.e. the contribution of each identified mode is calculated with respect to the measured PM_{10} mass concentration.

3.4.2. Optical properties at the surface

UV, visible and near infrared aerosol light absorption coefficients are measured with the AE-33 aethalometer. Ambient concentrations of eBC are then retrieved using data obtained at 880 nm and known mass absorption cross section coefficients (MACs). In this study site-specific MACs are experimentally determined using elemental carbon (EC) concentrations from PM_{10} samples collected at the same site. Our results indicate that the MAC at 880 nm at Aosta–downtown is 6.0 m^2 g^{-1}, i.e. lower than the default AE-33 value (7.77 m^2 g^{-1}), but in agreement with values reported for urban aerosols and externally mixed BC with little coating [83–85].

Afterwards, the measured eBC is apportioned into its fossil fuel (eBC_{ff}) and biomass burning (eBC_{bb}) contributions based on wavelength-dependent light absorption [86]. This method is critically sensitive to the AÅE assumed for fossil fuel and biomass burning ($AÅE_{ff}$ and $AÅE_{bb}$, respectively). Hence, the response of the "aethalometer model" is evaluated by varying $AÅE_{ff}$ and $AÅE_{bb}$ within a reasonable range [87]. The final coefficients are selected based on the results of the correlation analysis between the levoglucosan mass measured on site and the retrieved eBC_{bb}. Notably, the optimal AÅEs are chosen so that the regression line has intercept close to zero, under the assumption that both biomass tracers are removed from the atmosphere at a similar rate. During an intensive measurement campaign in 2018, this analysis gave the values $AÅE_{ff}$ = 1.1 and $AÅE_{bb}$ = 2.2, which are used here.

4. Results

We start this section with an assessment of the meteorological situation in 2020 compared to the five previous years (Sect. 4.1). Then, we examine the air quality changes to the reference scenario for both gaseous pollutants (Sect. 4.2) and PM (Sect. 4.3) at the surface. In order to explain the weaker reduction of aerosol concentrations compared, e.g., to nitrogen oxides, both source apportionment techniques (Sect. 4.4) and vertical column amounts/profiles (Sect. 4.5) are considered.

4.1. Meteorological context in 2020

We use the daily weather classification developed in one of our previous studies [45], based on the surface meteorological variables measured at the Aosta–Saint-Christophe station (chosen as representative of the wind flows at the bottom of the valley) to compare the occurrence of different weather patterns in 2020 with the previous years. Figures S1–S3 show the results from the classification, together with detailed information on air temperature and precipitation. It can be noticed that winter periods are generally characterised by wind calm, likely owing to strong temperature inversions in the lowest atmospheric layers and cloudy conditions. In the other periods of the year, the weather is dominated by easterly flows, driven by either the thermal circulation or synoptic forcing, and usually carrying air pollution from the Po basin. Days characterised by westerly winds and precipitation can occur, but they are less systematic – their frequency changing from year to year – and the geographical distribution of precipitation might be very heterogeneous. We list below the meteorological features encountered in 2020 that are relevant to the present study:

Preprints (www.preprints.org) | NOT PEER-REVIEWED | Posted: 28 June 2021 doi:10.20944/preprints202106.0667.v1

– P1 presents only few days with easterly winds, while westerly circulation is above average. Temperature in P1 during 2020 is also higher, on average, than the previous years;
– P2, P3, and P4 in 2020 feature more days than average with easterly winds (indeed, 2020 holds the record of the last years in P2 and P4);
– days in P5 with persistent westerly flows are more frequent in 2020 than average, while the opposite occurs for easterly winds. The total precipitation amount is larger than average in Aosta and Donnas;
– days with westerly flows are fewer than average in this period in 2020. Moreover, temperature in Aosta in P6 is lower than average. Thus, although precipitation is less abundant, snowfalls in Aosta are more frequent than average (about 9 days in 2020 compared to 1 day, e.g., in 2019 and 2018).

In addition to the local meteorological conditions, synoptical patterns leading to air pollution transport over the medium (e.g., from the Po basin) and long range (e.g., from the Sahara desert) must also be considered. The most relevant episodes occurring in 2020 are identified based on the examination of the ALC profiles, wind provenance and back-trajectories [44,45]:

– P1 is characterised by some episodes of advection of polluted air masses from the Po basin (for a total of 25 days, i.e. 37 % of the time in the period). Saharan dust is also transported on seven days overall in this period;
– P2 features an extraordinarily long series of transport episodes of fine particles from the Po basin (almost continuously from 14 March to 13 April, i.e. 88 % of the days), according to the frequent easterly wind flows mentioned above, and mineral dust from Sahara (mainly floating at some km from the surface without settling on the ground, but detected by the ALC and the sun/sky radiometer, Sect. 4.5). Within this period, moreover, we notice a remarkable and very unusual transport of dust particles from the area of the Caspian sea and Aral lake [e.g., 37] between 28 and 30 March, leading to instantaneous PM_{10} concentrations $> 50\ \mu g\ m^{-3}$ in Aosta–downtown, these particles being mostly concentrated in the coarse mode;
– during P3, transport from the Po basin occurs for a dozen days (62 %, according to the larger-than-usual frequency of easterly winds), with both fine and coarse particles involved (these latter likely still circulating from the previous long-range events);
– more than 50 % and about 45 % of the days are affected by advection of fine and coarse aerosol from the Po basin in P4 and P5, respectively. In line with the 2020 increase of westerly winds in P5, the latter fraction is lower than average for the summer-autumn months, which, in 2020, feature a long sequence of events in September (19 days continuously), but almost no episodes in October;
– finally, in about 38 % of the days in P6 the air quality in the Aosta Valley is impacted by transport of fine particles from the Po basin, although easterly winds are too weak and intermittent to be detected by our automatic weather pattern classification, while dust is identified (but not at the surface) on 3 days only.

4.2. Changes in surface gaseous pollutant concentrations

The statistical distributions of daily average gaseous pollutant concentrations in the different phases analysed in this study are represented in Fig. 3, for NO_2 as an example, and Figs. S4–S5 for NO and O_3, respectively, in comparison with the previous years. Nitrogen oxides exhibit a rather sharp decrease everywhere in 2020 and during the whole year, especially in periods P2 to P4, i.e. during the strict lockdown and the following phase of confinement within the region. The NO_x concentrations observed in 2020 are even lower than the ones registered in 2019, a year characterised by weather patterns particularly favourable to air pollutant dispersion. As already noticed in the scientific literature [e.g., 18,19], both the median of the concentrations and their variabil-

Preprints (www.preprints.org) | NOT PEER-REVIEWED | Posted: 28 June 2021 doi:10.20944/preprints202106.0667.v1

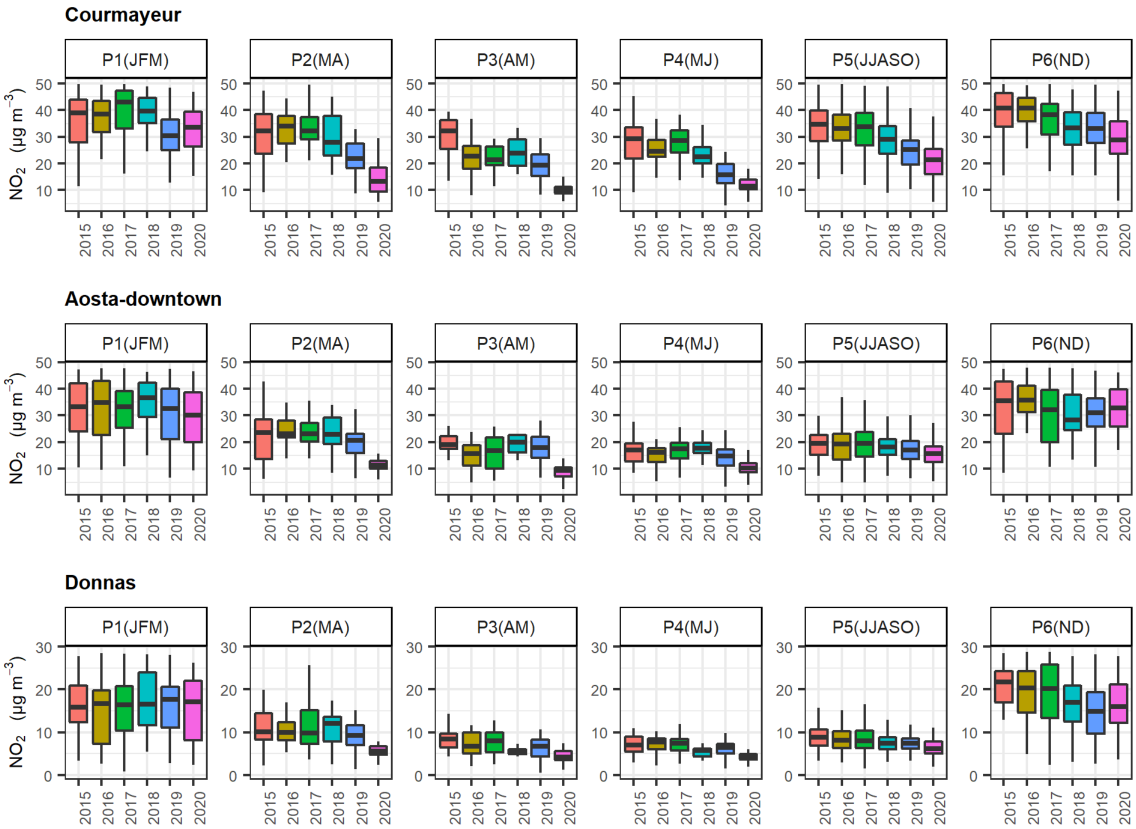

Figure 3. Median (horizontal line in the box), interquartile range (box height), overall variability excluding outliers (vertical line) of daily average NO_2 concentrations measured in each of the periods defined in Sect. 2.3 of the last six years at each air quality station. The month initials are reported in parentheses next to the period for better understanding. Notice that the range of the vertical scale is narrower for Donnas for better visualisation. Similar plots for other gaseous pollutants are included in Sect. S4 of the Supplementary Materials.

Preprints (www.preprints.org) | NOT PEER-REVIEWED | Posted: 28 June 2021 doi:10.20944/preprints202106.0667.v1

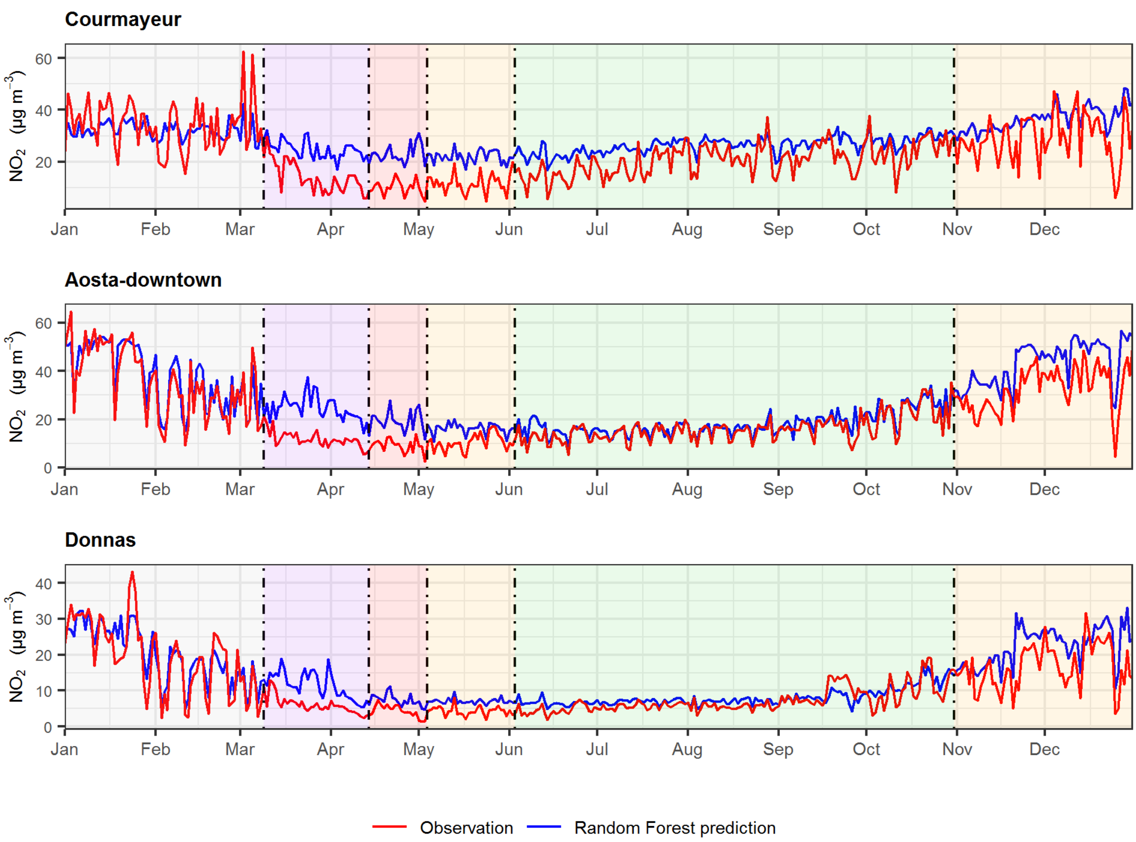

Figure 4. Observation (red) and prediction with the random forest algorithm (blue, counterfactual reference) of NO_2 surface concentrations for year 2020. The vertical scales are different for ease of visualisation. Similar plots for other gaseous pollutants are included in Sect. S4 of the Supplementary Materials.

 doi:10.20944/preprints202106.0667.v1

ity decrease, owing to the weakening of the emissions and their periodic modulation. Changes in ozone, on the other hand, are much more limited.

An even better detail can be captured by observing the 2020 yearly evolution of the measured gas concentrations and the output of the predictive statistical model, representing the counterfactual reference. These are shown in Fig. 4, for NO_2 as an example, and Figs. S6–S7 for NO and O_3. An overall good agreement between the measured and predicted NO_x data sets can be noticed before the beginning of the restrictions, in P1. An abrupt split of the curves occurs after the establishment of the confinement regulations, in P2–P4, and again in P6. While in Aosta–downtown and Donnas the difference between the NO_x observations and the counterfactual scenario tends to decrease and to vanish in P5, a negative offset persists in Courmayeur, likely due to the influence of international road traffic, still 15–20 % lower than usual, and to the exceptional occurrence of westerly winds, not fully compensated by the random forest.

The results for O_3 are less clear and more difficult to interpret. In P2–P3, we observe an increase in Aosta–downtown, compared to the counterfactual scenario, and a decrease in P2 in Donnas. A possible reason for this contrasting behaviour could be that reduced titration by NO triggers an ozone increase in the urban environment of Aosta, while reduced precursors contribute to a decrease at the Donnas rural station, as also found at other remote Italian sites [88]. However, in contrast to P2–P3, O_3 concentrations slightly decrease in Aosta–downtown in P6 (more evident in Fig. 7). This can be explained in the following way. Ozone production in winter owing to photochemistry is negligible and the only phenomena contributing to wintertime O_3 increase in the Aosta Valley are Foehn winds, which bring ozone-rich air masses from higher altitudes down to the surface. Since in 2020 westerly circulation was much weaker than the previous years in P6, the ozone concentrations are also lower than usual. However, it must be considered that O_3 absolute concentrations are much lower in winter compared to P2–P3 (e.g., Fig. S7), and the relative changes are probably not significant. Finally, it should be noticed that, in Donnas, the largest difference between the observed O_3 concentrations and the ones predicted by the random forest occurs in P5. This is consistent with the overall O_3 negative anomaly detected in northern Italy in summer 2020 [88], especially considering the proximity of Donnas to the Po basin.

The reductions of gaseous pollutant concentrations estimated by all methods previously described (Sect. 3), including CTMs, are quantified and compared in Figs. 5–7 for NO, NO_2, and O_3, respectively. The reduction in NO concentrations with respect to the previous years' average reaches -60 % everywhere in P2, very homogeneously despite the wide range of absolute variations (-0.5 µg m^{-3} in Donnas, -4.5 µg m^{-3} in Aosta–downtown, and -9.1 µg m^{-3} in Courmayeur), and also in P3 in Courmayeur (-5.9 µg m^{-3}) and Aosta–downtown (-3.7 µg m^{-3}). Values as low as -50 % (-6.6 µg m^{-3}) in Courmayeur persist even in P4. For NO_2, the decrease compared to the previous years is slightly weaker, but still important, reaching -40 % or even -50 % in P2–P4 (e.g., -14.6 µg m^{-3} in Courmayeur, -9.0 µg m^{-3} in Aosta–downtown, and -3.9 µg m^{-3} in Donnas). The new decrease in P6, at the end of the year, amounts to about -40 % to -60 % for NO (-9.5 µg m^{-3} in Courmayeur, -17.4 µg m^{-3} in Aosta–downtown, and -4.4 µg m^{-3} in Donnas) and to -20 % to -30 % for NO_2 (-10.2 µg m^{-3} in Courmayeur, -8.5 µg m^{-3} in Aosta–downtown, and -6.7 µg m^{-3} in Donnas). As already mentioned, a remarkable reduction of about -40 % (-7.9 µg m^{-3}) for NO and -30 % (-8.8 µg m^{-3}) for NO_2 relative to the average of previous years is also found during P5, in Courmayeur. The predictive statistical model provides similar results compared to the anomaly calculations with respect to the previous years, even enhancing the NO_x reductions found for periods P2–P4. Hence, the weather-compensated NO changes reach -80 % (-1.2 µg m^{-3}) in Donnas in P2 and -70 % (-8.3 to -6.1 µg m^{-3}) in Aosta–downtown (P2–P3), with still important decreases in P4 and P6, and the NO_2 reductions touch -50 % everywhere (-13.0 µg m^{-3} in Courmayeur, -12.6 µg m^{-3} in Aosta–downtown, and -5.4 µg m^{-3} in Donnas).

Preprints (www.preprints.org) | NOT PEER-REVIEWED | Posted: 28 June 2021 doi:10.20944/preprints202106.0667.v1

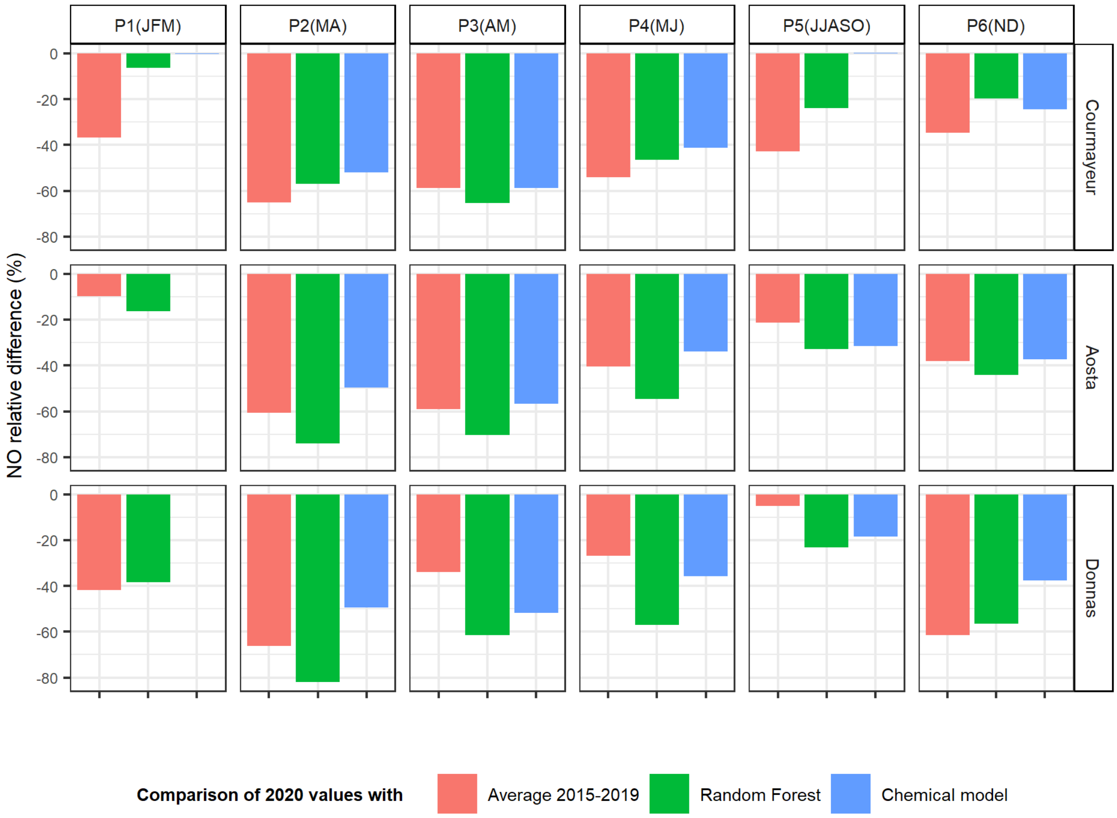

Figure 5. Changes in NO surface concentrations compared to the reference scenario (average of previous years, counterfactual modelling), according to the three analysis methods described in the study.

Preprints (www.preprints.org) | NOT PEER-REVIEWED | Posted: 28 June 2021 doi:10.20944/preprints202106.0667.v1

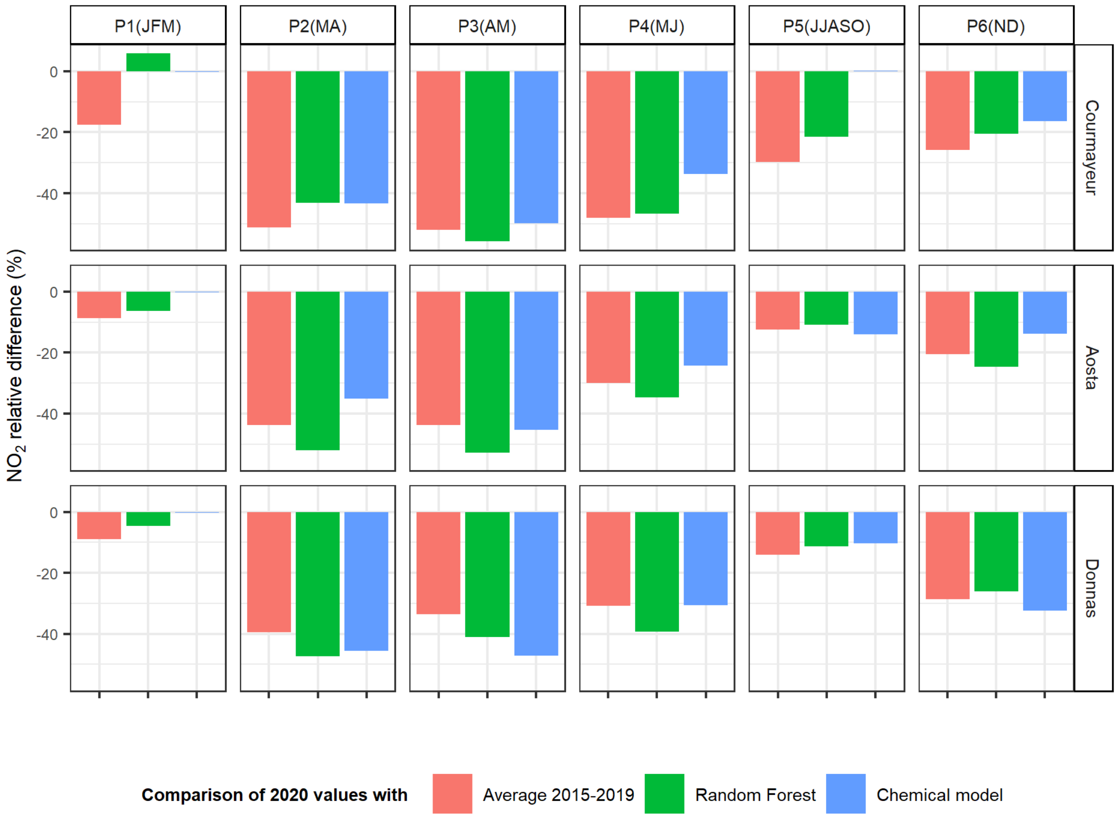

Figure 6. Changes in NO_2 surface concentrations compared to the reference scenario, according to the three analysis methods described in the study.

Figure 7. Change in O_3 surface concentrations compared to the reference scenario, according to the three analysis methods described in the study.

Preprints (www.preprints.org) | NOT PEER-REVIEWED | Posted: 28 June 2021 doi:10.20944/preprints202106.0667.v1

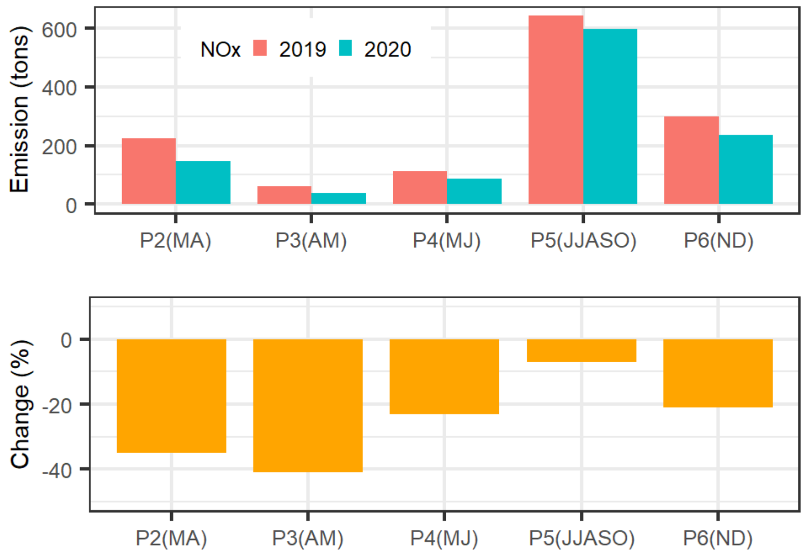

Figure 8. Total NO_x emissions in the model domain for the reference and curtailed scenarios. P1 is left unchanged, since it is prior to the lockdown measures. Similar plots for PM_{10} are included in Sect. S5 of the Supplementary Materials.

The CTM follows rather well the effect of the lockdown on NO_x already outlined by the predictive statistical model, with differences generally within 10–20 % to this latter. A few exceptions, with differences between the predictive statistical model and the CTM larger than 20 %, are visible in Donnas (P1–P2, and P4), in Aosta (P2 and P4), and in Courmayeur (P5). However, it should be kept in mind that NO_x concentrations are very low in summer and that the complex orography (e.g., in the vicinity of the Mt. Blanc massif) could lead to systematic differences between the CTM and measurements at the bottom of the valley. Overall, the CTM responds closely to the reductions of NO_x emissions provided by the inventory, which are represented in Fig. 8 (notice that our inventory only includes NO_x emissions, which are partitioned at a second stage into NO, NO_2 and O_3 by FARM). The reductions amount to 35–40 % in P2–P3, and to 20 % in P4 and P6, on average, in the Aosta Valley. The results for O_3 are the most divergent ones and the various methods show changes differing in both magnitude and sign. They highlight the challenge of interpreting and modelling the behaviour of this secondary compound, depending on both meteorological and complex chemical mechanisms. The relative differences, however, are generally within 20 %, which approaches the uncertainty of all used techniques, with the exception of P5 in Donnas and P6 in Aosta (these cases were already discussed above). Since FARM only accounts for changes in local emissions, it responds to the decreasing NO_x with an increase of O_3.

4.3. Changes in surface PM concentrations

Absolute PM concentrations in 2020 and in the previous five years are plotted in Figs. S8–S9. Particle matter does not show the large changes found for NO_x during the strict lockdown periods. Indeed, $PM_{2.5}$ even slightly increases compared to average in P2–P4 and P6 (the reason will be clear in the next paragraphs). Year-to-year PM_{10} variations often show similar modulations at different stations, due to the effect of large-scale weather patterns [45] and long-range aerosol transport affecting different sampling sites in about the same way. For example, minimum PM concentrations are found in 2019 due to the aforementioned particular meteorological conditions in that year.

A comparison of daily PM observations and their respective predictions with the random forest technique is shown in Figs. S10–S11 for $PM_{2.5}$ and PM_{10}, respectively,

Preprints (www.preprints.org) | NOT PEER-REVIEWED | Posted: 28 June 2021 doi:10.20944/preprints202106.0667.v1

Figure 9. Change in $PM_{2.5}$ surface concentrations in Aosta–downtown compared to the reference scenario, according to the three analysis methods described in the study.

while Figs. 9 and 10 show their relative changes to the reference scenario. Compared to the previous years' average, $PM_{2.5}$ increases by about 5–10 % in P2 and P4 (0.9–0.5 µg m^{-3}), and – slightly less (4 %, i.e. 0.7 µg m^{-3}) – in P6. However, if meteorology is taken into account, as in the predictive statistical model, remarkable reductions – as large as 20 % (e.g., -1.8 µg m^{-3}) – are found, indicating that the weather plays a major role. During the lockdown phases in the earlier part of the year, PM_{10} generally decreases, e.g. in P2–P3 in Aosta (-10 to -25 %, i.e. -1.6 to -5.4 µg m^{-3}, depending on the method, but identified by all analysis techniques) and in P3–P4 in Courmayeur (-1.8 to -2.4 µg m^{-3}). From the comparison, in Aosta–downtown, between $PM_{2.5}$ (increasing) and PM_{10} (decreasing) in the first lockdown (P2), it is clear that the aerosol size range contributing to most of the PM reductions lies between 2.5 and 10 µm. Indeed, $PM_{2.5-10}$ decreases by more than 50 % (about 3 µg m^{-3}) in P2 compared to the 2015–2019 average (not shown), and the reduction would have been even larger if dust transport from the Caspian sea (Sect. 4.1) had not occurred in the same period. In Courmayeur and Donnas, the largest reductions are actually seen in summer (P5) and may be due to weaker long-range transport of aerosol compared to average (Sect. 4.5). Since large-scale dynamics are not included in the random forest parametrisation, the evaluation of changes with the predictive statistical model is close to the anomaly calculation for similar weather conditions. An exception is represented by P1 at all sites, and notably in Courmayeur, where comparison with the statistical model provides a larger increase compared to the anomaly calculation. Based on the analysis of volume size distributions in Courmayeur (Sect. 4.4), the most likely explanation is the influence of dust transport and deposition, coupled to weather conditions normally reducing PM_{10} concentrations. Conversely, since these dynamics are included in both the reference and perturbed scenario in the CTM (unaltered boundary conditions), the reduction due to the cleaner conditions in 2020 (P5) is not reproduced by FARM, which only accounts for variations of local emissions. Anyway, the overall picture is rather consistent with the reduction in PM emissions according to the regional inventory (Fig. S12), but aerosol concentrations are more perturbed by large-scale dynamics than gaseous pollutants.

4.4. Aerosol source apportionment

Four variation modes can be very clearly identified from size-PMF and are able to reconstruct the PM_{10} concentration with a correlation index of 0.995, negligible offset (0.3 µg m^{-3}) and slope of 0.98. Their profiles are remarkably similar at all sampling sites equipped with a Fidas200E particle spectrometer and are shown in Figs. S13–S16. As already discussed in a previous study [45], the accumulation mode with the smallest size (centred at about 0.2 µm) is linked to particles formed through condensation/coagulation

Preprints (www.preprints.org) | NOT PEER-REVIEWED | Posted: 28 June 2021 doi:10.20944/preprints202106.0667.v1

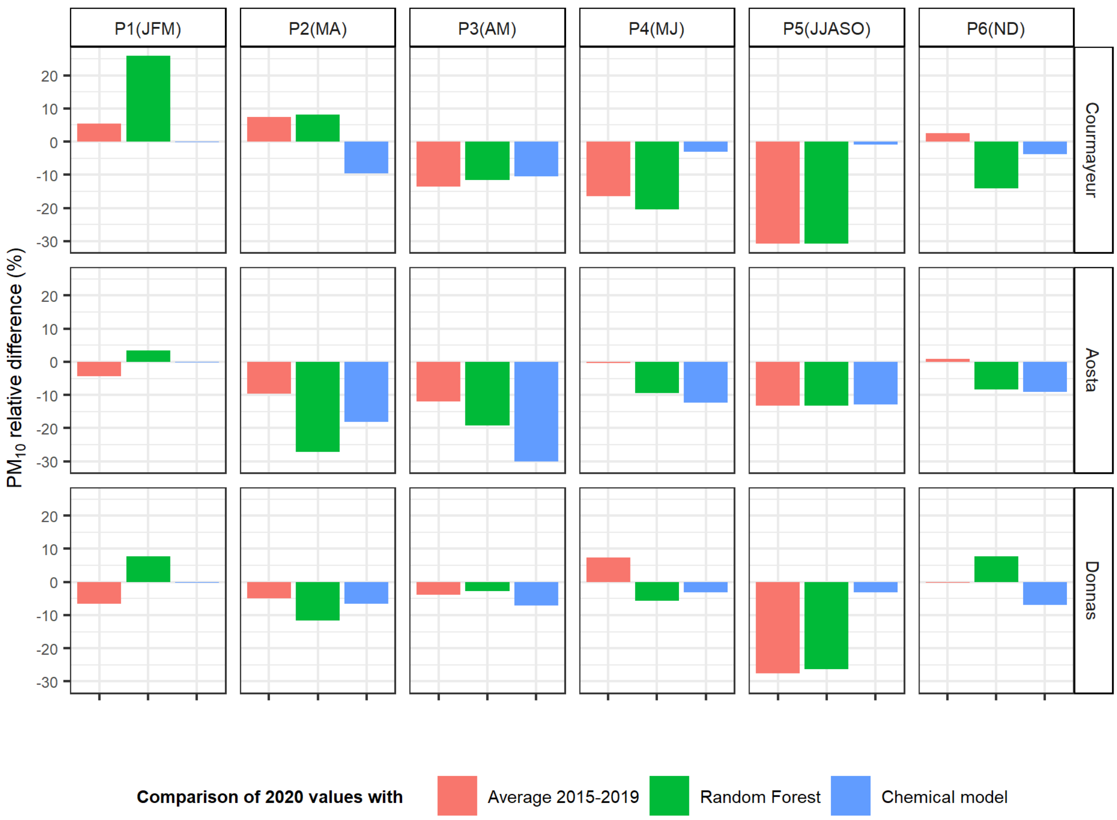

Figure 10. Change in PM_{10} surface concentrations compared to the reference scenario, according to the three analysis methods described in the study.

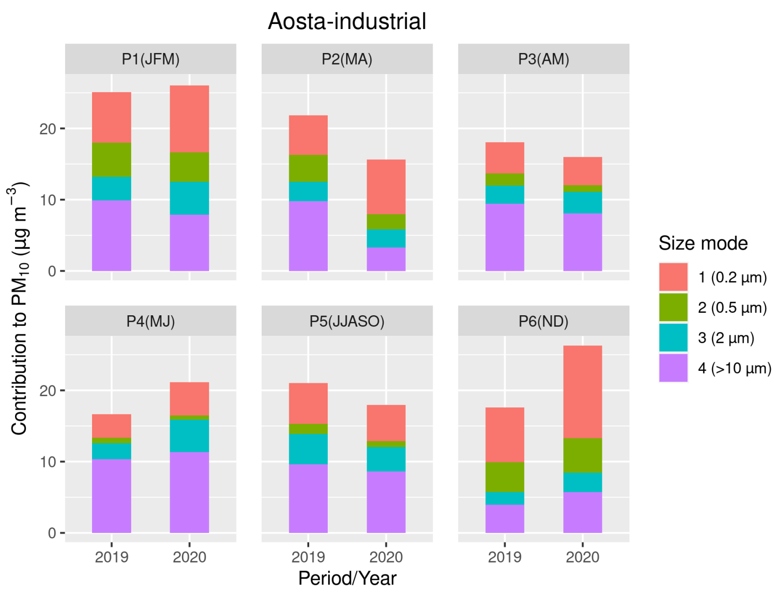

Figure 11. Contribution to the PM_{10} concentration measured at the Aosta–industrial station by the four modes identified with size-PMF. Only periods with full data coverage are shown in the plot.

Preprints (www.preprints.org) | NOT PEER-REVIEWED | Posted: 28 June 2021 doi:10.20944/preprints202106.0667.v1

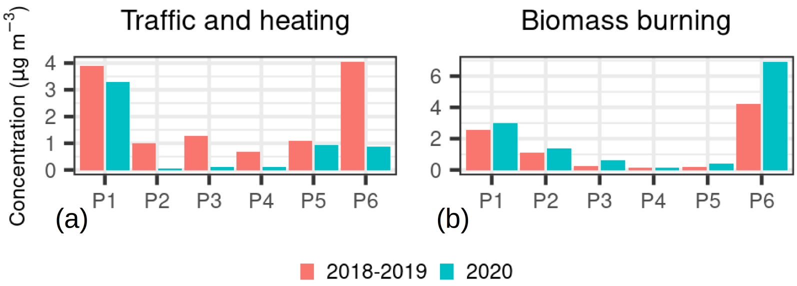

Figure 12. Contribution of (a) non-biomass combustion processes (e.g., traffic and heating) and (b) the biomass burning mode to the PM_{10} concentration in Aosta–downtown from chem-PMF based on anion/cation, EC/OC, and levoglucosan. Notice that the range of the vertical axes in the subfigures differs for ease of visualisation.

processes and aging ("condensation mode"), such as sulfates transported from the Po basin and aerosol originated from traffic exhaust and heating. The slightly larger accumulation mode, centred at about 0.5 µm ("droplet mode"), is representative of the nitrate particles forming in aqueous-phase processes, e.g. in fog during the cold season. The third mode correlates remarkably well with mineral dust deposition, and possibly its resuspension. This is confirmed by comparing its evolution with the results of desert dust forecasts (NMMB/BSC-Dust, http://ess.bsc.es/bsc-dust-daily-forecast, last access: 22 June 2021) and the analysis of back-trajectories, ALC profiles and volume size distributions from the sun/sky radiometer. The mode is centred at about 2 µm, a size consistent with dust dry deposition [89,90]. Finally, the fourth mode is coarse, with size > 10 µm, and is representative of the largest particles such as the ones resuspended from soil and de-icing road salt.

The size-PMF output is shown in Fig. 11 for the Aosta–industrial station and in Figs. S17–S18 for Courmayeur and Aosta–downtown/Saint-Christophe. Although the series are not long enough to allow us compare the 2020 anomaly with a longer-term average, we can anyway point out some microphysical characteristics of the aerosol in the Aosta Valley. First, fine particles (modes 1–2) are significant contributors to the total mass at all sites. Since their origin is both local and remote, this highlights the importance of monitoring and accounting for air mass transport, notably in the wintertime lockdown periods (P2 and P6). Likewise, owing to the decrease of easterly winds in P5, the contribution of fine particles, and even of the third mode (mineral dust), is lower than usual in that period. Aosta–industrial (Fig. 11) represents an interesting case, witnessing in P2 (i.e., when the industrial plant is closed) a remarkable reduction of the coarse (> 10µm) fraction, which is mainly coming from fugitive emission from the steel mill and, to a less extent, from car traffic. This is particularly interesting, since – as already noticed in Sect. 4.3 – the main contribution to PM reductions in Aosta–downtown in P2 (compared to the 2015–2019 average) is in the 2.5–10 µm size range (further insights are provided by chem-PMF). As soon as the steel mill resumes normal operation, the coarse particles increase again. Mineral dust is especially important in P3 in 2018 (from data collected in Courmayeur and Aosta–Saint-Christophe), which explains the large PM_{10} concentrations in that period and year. As a final remark, coarse particles from de-icing road salt are very important at the Courmayeur traffic station in P1 and P6, and in Aosta in P6 in 2020, since this latter was a particularly snowy winter.

Several factors emerge from chem-PMF in Aosta–downtown depending on the considered variable subset. All chem-PMF factorisations are able to reconstruct the PM_{10} series with a correlation coefficient > 0.94 and only few swaps. Six factors are found from the decomposition using anion/cation, EC/OC and levoglucosan (Fig. S19): de-icing road salting (with high concentrations of Na and Cl), biomass burning (high levoglucosan and medium EC and OC), non-biomass burning combustion processes

 doi:10.20944/preprints202106.0667.v1

such as traffic/heating (with high EC and NO_x), two modes related to transport of secondary particles from the Po basin (rich in nitrate and sulfate, respectively [44,45]), and a mode rich in crustal elements, such as Ca and Mg. This latter may be connected with both resuspension by traffic/wind and emission from industry. Indeed, oxides of Ca, Si, and Fe originate as slags from the electric arc furnace employed in the steel mill. Moreover, Ca, Si, Al, and Mg oxides form from refining treatments in the ladle furnace. These elements are present in the coarse fraction of fugitive emissions from the industrial plant and are believed to contribute to the "soil" mode at the Aosta–downtown station. When metals are included in chem-PMF, seven factors arise (Fig. S20): road salt, combustion processes, secondary sulfate, secondary nitrate, soil, and two factors respectively rich in heavy metals (e.g., Cr, Ni, and Mo) from the steel mill, and a Cd- and Pb-rich mode, which was attributed to the industrial sector in a previous study [45]. Cu is found in similar quantities in both traffic and soil modes, which is a possible clue of the contribution of traffic to soil resuspension.

From the first factorisation, we show the evolution of non-biomass and biomass combustion processes in Fig. 12. An almost total reduction of the first mode in the confinement periods (P2–4, and P6) in 2020, compared to the previous years (average from 2018–2019, for this data set), is visible, which can be assigned unambiguously to the reduction of traffic. Also notice a minor reduction during P1, likely due to higher temperatures and less domestic heating in 2020. Conversely, biomass burning shows a slight increase in P2 and a large increase in P6. However, when normalised to the total $PM_{2.5}$ concentration (Fig. S21) we see that such mode actually decreases (in P2) or does not change (in P6) in percentage compared to the previous years, indicating the more important influence of meteorology and air mass transport, as already found using the random forest technique in Sect. 4.3 for $PM_{2.5}$ and PM_{10}. These conclusions are additionally supported by the optical source apportionment. Figure S22 shows that, despite the reduction of absolute eBC concentrations (and notably, their peak values) in P2 and P6 due to mobility restrictions, the ratio eBC_{ff}/eBC is only marginally (by about -10 %) affected, and is still shifted to higher fossil fuel ratios. Hence, the role of biomass burning in counterbalancing the PM reductions during the confinement period is rather limited in Aosta–downtown compared to what has been hypothesised in other Italian regions [25,34]. However, in smaller villages of the Aosta Valley, where wood combustion is a more common practice, the importance of biomass burning emission may be greater.

Likely connected to the traffic reduction and to the shutdown of the steel mill, the soil mode also shows an important reduction in P2 compared to the 2017–2019 average (Fig. 13a), as well as a general decrease during the whole year, due to both a decrease of the sources and the meteorological conditions (e.g., in P5). This likely represents the missing source in the 2.5–10 μm size range mostly contributing to the reduction of the PM mass concentration in P2 in 2020. The closure of the industrial plant also reverberates on the metal concentration in Aosta–downtown, as apparent from Fig. 13b. Interestingly enough, although the concentrations of Cd and Pb completely drop at the Aosta–industrial station, the respective Cd- and Pb-rich PMF mode in Aosta–downtown does not decrease relevantly (not shown), possibly indicating an additional source in the city. A secondary minimum in the chem-PMF "industry" mode, driven by heavy metals, occurs in P5, likely owing to the decreased activity of the steel mill in summer 2020 and to meteorological conditions unfavourable to the detection of industrial emissions at the Aosta–downtown station. As opposed to the soil and traffic modes, the nitrate- and sulfate-rich modes remarkably increase in P2 compared to the previous years (Figs. 13c–13d). This is almost certainly due to the anomalous frequency of easterly winds in the same period in 2020 (Sect. 4.1), which bring polluted air masses from the Po basin to the Aosta Valley. However, an increase in secondary aerosol production in the urbanised source regions of the Po basin due to the enhanced atmospheric oxidising capacity [e.g., 91] cannot be excluded. Finally, meteorology – and, notably, more frequent

Preprints (www.preprints.org) | NOT PEER-REVIEWED | Posted: 28 June 2021 doi:10.20944/preprints202106.0667.v1

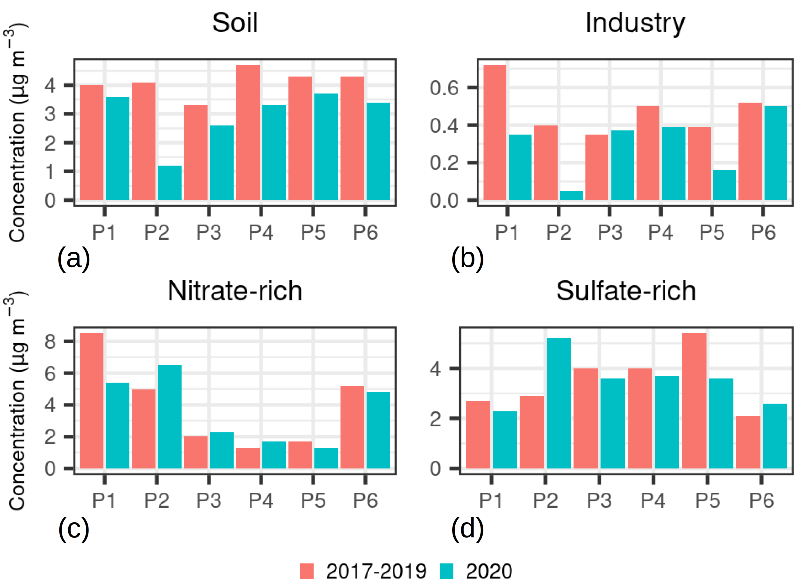

Figure 13. Contribution of the most relevant modes to the PM_{10} concentration in Aosta–downtown from chem-PMF based on anion/cation and metals. Notice that the average period is extended compared to Fig. 12 and that the range of the vertical axes in the subfigures differs for ease of visualisation.

westerly winds in 2020 – is also the most reasonable explanation of lower-than-usual concentrations of fine particles during P5.

4.5. Vertical profiles and column amounts

Since P3 is characterised by higher-than-usual precipitation and cloudiness (Sect. 4.1), which hampers retrievals with both the sun/sky radiometer and the ALC, and since P3 is rather short, in this final section we merge P2 and P3 in a single period.

The 2020 anomaly in the total NO_2 vertical column detected by the Brewer spectrophotometer is shown in Fig. 14. This closely resembles the results obtained at the surface in Aosta–downtown (Fig. 6). In particular, the NO_2 maximum reductions in P2–3 and P6 also seen at the surface are correctly reproduced over the column, albeit with different intensities. This is to ascribe to the fact that stratospheric NO_2 (unperturbed by surface changes) is maximum in summer, and represents a relevant part of the vertical column over the Aosta Valley, while the tropospheric column dominates the total NO_2 VCD in winter. This is likely the reason why in P4 we do not detect large variations compared to the previous years, in contrast to surface measurements. Finally, NO_2 VCDs decrease in P1. This is also noticed in surface concentrations and could be attributed to reduced NO_x emissions by domestic heating systems owing to higher temperatures (Sect. 4.1), and to decreased easterly winds possibly transporting some NO_2 in the tropospheric column [45].

The relative anomaly in PM concentrations retrieved by the ALC along the vertical profile is depicted in Fig. 15, which reveals some interesting details. First of all, in almost every period the aerosol load in the elevated layers above the surface are larger in 2020 than in the previous years, likely due to increased long-range particle transport (Sect. 4.1). Only P5 proves to be a relatively clean period in 2020 compared to average, which is the reason of the remarkable PM reductions detected at the various stations in May and June 2020 despite unperturbed emissions (Fig. S12). This overall evolution along the vertical column is fully confirmed by the aerosol optical depth from the sun/sky radiometer (Fig. S23), showing larger-than-usual AODs in all periods except P5. Once again, this analysis demonstrates that long-range transport can interfere, and should be

 doi:10.20944/preprints202106.0667.v1

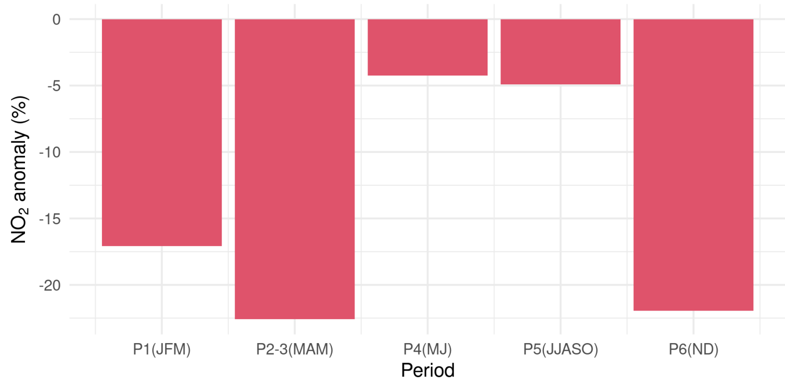

Figure 14. 2020 anomaly in NO_2 VCDs compared to the previous years as detected from the Brewer spectrophotometer over the whole atmospheric column.

accounted for, in the determination of the effects from varying surface emissions, and that column or profile measurements are effective in identifying such situations. Even more interestingly, in the periods affected by the lockdown restrictions (P2–3, P4, and P6), we notice from Fig. 15 some reductions of the PM mass concentration in the layers close to the ground, despite the overall increase of the aerosol load in the atmosphere. These reductions are mostly concentrated during the day, and notably during the rush hours when the greatest decreases of aerosol emissions at the surface are expected due to the confinement measures. The diurnal valley convection could then favour mixing of this cleaner air, with effects visible up to about 1000 m a.s.l., i.e. some hundreds of metres above the surface.

5. Discussion and conclusions

The present study analysed the effect of the COVID-19 confinement regulations on air quality in the northwestern Alps. Five sites in the Aosta Valley were selected, characterised by different environmental conditions: a traffic station next to the Mt. Blanc tunnel (Courmayeur), an urban background site in the main settlement of the region (Aosta–downtown), a sampling site close to a steel mill (Aosta–industrial), a semi-rural location (Aosta–Saint-Christophe), and a rural station at the border with the Po basin (Donnas). Data from 2020 (from winter to winter) and the previous years (back to 2015, depending on the considered data set), collected with different techniques both at the surface (trace gas and aerosol mass concentrations, fine characterisation of the microphysical, chemical and optical aerosol properties) and in the vertical column (NO_2 vertical column amounts, aerosol optical depth, and PM concentration profiles), were studied and some of them were compared to the output of two different types of models (a statistical predictive model based on the random forest algorithm and a deterministic chemical transport model).

Based on the research questions mentioned in the introduction, we can now draw the following conclusions.

- Q1–3: changes in air pollutant concentrations, their magnitude, sign, and sources. At all examined stations, even the rural ones, relevant changes in air quality resulting from the confinement regulations can be identified. The largest variations occur for NO_x, due to curtailed emissions from vehicular traffic. NO decreases by 70–80 % in March–May 2020 and by 20–60 % in November–December, depending on the site, while NO_2 decreases slightly less, by about 50 % and 20–30 % in the two periods, respectively. These values agree with the results from previous studies in northern Italy and in other locations worldwide. The secondary decrease at the beginning of the 2020–2021 winter season also highlights the importance of considering, as done here, a data set encompassing both the first and the following pandemic waves

Preprints (www.preprints.org) | NOT PEER-REVIEWED | Posted: 28 June 2021 doi:10.20944/preprints202106.0667.v1

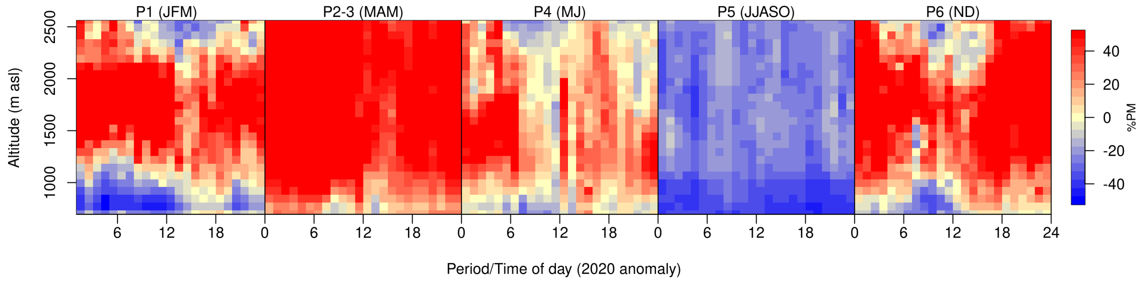

Figure 15. 2020 relative anomaly in PM profiles compared to the previous years as detected from the ALC. Every subfigure represents an "average day" (from 0 to 24 UTC) for the different periods.

and the corresponding regulations. Among trace gases, ozone does not show any relevant increase, contrary to what has been found in spring 2020 in more urbanised areas. Instead, O_3 variations are modest and of different sign depending on the examined period and location, and are likely affected by meteorology, e.g. Foehn winds bringing ozone-rich air masses from higher altitudes to the surface, and by atmospheric exchanges with the Po basin.
Particle matter concentrations show maximum variations only up to 25 % (when taking meteorology into account) due to their multifaceted nature. Notably, as found from the analysis of the aerosol microphysical properties (size distributions), fine particles represent a large fraction of the aerosol mass in the Aosta Valley and they increase during the lockdown periods due to intensified easterly winds (from the Po basin) in 2020 compared to the average of previous years, as also confirmed by remote measurements along the vertical column. Although not explicitly proven here, enhanced secondary aerosol production in their source area, in addition to meteorology, could contribute to the observed increase. Based on the optical source apportionment and chemical speciation, no relevant increase in biomass burning emissions from residential heating due to stay-at-home policies is observed in Aosta–downtown, although conditions in more rural areas might be different. Conversely, the mass concentration of the largest particle decreases, as a result of reduced resuspension by traffic, and, in Aosta, of the shutdown of the steel mill, as confirmed by the aerosol chemical speciation.
A limitation of this study is the availability of only measurements from stations located at the bottom of the valley, whereas no high-altitude station is yet available in our network to check if the air quality is influenced by the lockdown even there. As a partial integration, the analysis of vertical column with remote sensing instrumentation shows that the aerosol profiles are mostly influenced by long-range transport of desert dust or secondary aerosol from the Po basin, with the possible exception of a very shallow layer close to the surface, about 500 m thick, where we see negative concentration anomalies in correspondence to rush hours and mixing layer development. This aspect should be explored in more depth, and in a wider context, in future research. Conversely, the NO_2 vertical column is strongly impacted by the lockdown, following similar changes as the ones found at the surface.

- Q4: agreement between observations and models. A predictive statistical model was proven to work well with NO_x and PM, with correlation indices generally > 0.9 and > 0.7, respectively. The results are useful to take the effects of weather into consideration and to decouple meteorology and emissions. The deviations between the measured concentrations in 2020 and the output of the statistical model (representing the counterfactual scenario needed for the analysis) were compared with the difference between the output of the FARM chemical transport model run with a curtailed and with a standard emission scenario. For NO_x and PM the comparison of the two methods provides comparable relative changes of

 doi:10.20944/preprints202106.0667.v1

concentrations due to the lockdown, thus confirming that both emission sources and processes are well represented by the modelling chain, and that the reasons of the observed variations are well understood. For O_3, the effect of the lockdown resulting from the statistical predictive model and the chemical transport model even differs in sign. This could be due to meteorological phenomena not taken into account in the same way by both methods, and to the influence of atmospheric dynamics acting on a wider scale, e.g. over the whole northern Italy. However, even for O_3 the deviations between the concentration changes assessed by the statistical and the deterministic models are generally within 10–20 %.

- Q5: influence of meteorology. The peculiar weather phenomena occurring in mountain valley regions, such as thermally-driven circulation and Foehn winds, turned out to be relevant in this investigation, as well as larger-scale dynamics for aerosol transport. For example, without accounting for the increase in easterly winds, bringing secondary aerosol in the valley during the period from March to June, the effect of the lockdown regulations on PM would have been underestimated. Similarly, without taking the frequent westerly winds in summer-autumn into account, the effect of the reduced traffic would have been overestimated. Finally, some of the observed O_3 changes could not have been understood without a reference to meteorology. The random forest approach provides a very useful framework to quantitatively assess the relative importance of meteorological variables on air quality. Profiling instruments and retrievals of column amounts are helpful tools to identify long-range transport and to correctly interpret observations at the surface and their changes.

Overall, this study highlights that even apparently pristine sites as the Alpine valleys are not free from air pollution, and that a further effort should be done to identify and cut the emission sources on different spatial scales. This also prompts the establishment of new and equipped measurement stations in high-altitude and remote areas, not directly affected by local emissions.

Author Contributions: Conceptualisation, H.D., T.M., G.P., C.T., and M.Z.; methodology, formal analysis and visualisation, H.D. and T.M.; data curation, H.D. (column/profile measurements), T.M. (meteorological data and statistical modelling), G.P. (chemical transport modelling), C.T. (air quality data), I.K.F.T. (light absorption properties), and G.F. (aerosol optical depths); supervision: M.Z.; writing—original draft preparation, H.D. and T.M.; writing—review and editing: all authors. All authors have read and agreed to the published version of the manuscript.

Funding: The participation of G.F. in this study is funded by Fondazione CRT in the frame of the Solar UV Extensive Network for Information and Reporting (SOUVENIR) project. I.K.F.T. is supported by the PREPAIR project (LIFE15 IPE IT013).

Data Availability Statement: Publicly available data sets were analysed in this study. The measurements from the ARPA Valle d'Aosta air-quality surface network can be found on the web page http://www.arpa.vda.it/it/aria/la-qualità-dell-aria/stazioni-di-monitoraggio/inquinanti-export-dati. The weather data can be retrieved from http://cf.regione.vda.it/richiesta_dati.php upon request to Centro Funzionale della Valle d'Aosta. The ALC data are available upon request from the Alice-net network (http://www.alice-net.eu/). The sun/sky radiometer data can be downloaded from the Skynet/Europe network web site (http://www.euroskyrad.net/index.html). Any other data can be requested to the corresponding author (h.diemoz@arpa.vda.it).

Acknowledgments: The authors are grateful to M. Pignet and S. Drigo for their technical support to the operation of the air quality network. They also acknowledge the laboratory of ARPA for the chemical analyses of PM_{10} samples, the European Cooperation in Science and Technology (COST) action "PROBE" (CA18235) for the valuable discussions leading to advancements in the use of the automated lidar ceilometer, and M. Hervo for calculating the ALC overlap correction model.

Conflicts of Interest: The authors declare no conflict of interest.

References

1. Amendola, A.; Bianchi, S.; Gori, M.; Colzani, D.; Canuti, M.; Borghi, E.; Raviglione, M.; Zuccotti, G.V.; Tanzi, E. Evidence of SARS-CoV-2 RNA in an Oropharyngeal Swab Specimen, Milan, Italy, Early December 2019. *Emerg. Infect. Dis. J.* **2021**, *27*, 648. doi:10.3201/eid2702.204632.
2. La Rosa, G.; Mancini, P.; Bonanno Ferraro, G.; Veneri, C.; Iaconelli, M.; Bonadonna, L.; Lucentini, L.; Suffredini, E. SARS-CoV-2 has been circulating in northern Italy since December 2019: Evidence from environmental monitoring. *Sci. Total Environ.* **2021**, *750*, 141711. doi:10.1016/j.scitotenv.2020.141711.
3. Le Quéré, C.; Jackson, R.B.; Jones, M.W.; Smith, A.J.P.; Abernethy, S.; Andrew, R.M.; De-Gol, A.J.; Willis, D.R.; Shan, Y.; Canadell, J.G.; Friedlingstein, P.; Creutzig, F.; Peters, G.P. Temporary reduction in daily global CO2 emissions during the COVID-19 forced confinement. *Nat. Clim. Change* **2020**, *10*, 647–653. doi:10.1038/s41558-020-0797-x.
4. Liu, Z.; Ciais, P.; Deng, Z.; Lei, R.; Davis, S.J.; Feng, S.; Zheng, B.; Cui, D.; Dou, X.; Zhu, B.; Guo, R.; Ke, P.; Sun, T.; Lu, C.; He, P.; Wang, Y.; Yue, X.; Wang, Y.; Lei, Y.; Zhou, H.; Cai, Z.; Wu, Y.; Guo, R.; Han, T.; Xue, J.; Boucher, O.; Boucher, E.; Chevallier, F.; Tanaka, K.; Wei, Y.; Zhong, H.; Kang, C.; Zhang, N.; Chen, B.; Xi, F.; Liu, M.; Bréon, F.M.; Lu, Y.; Zhang, Q.; Guan, D.; Gong, P.; Kammen, D.M.; He, K.; Schellnhuber, H.J. Near-real-time monitoring of global CO2 emissions reveals the effects of the COVID-19 pandemic. *Nat. Commun.* **2020**, *11*, 5172. doi:10.1038/s41467-020-18922-7.
5. Rodríguez-Urrego, D.; Rodríguez-Urrego, L. Air quality during the COVID-19: PM2.5 analysis in the 50 most polluted capital cities in the world. *Environ. Pollut.* **2020**, *266*, 115042. doi:10.1016/j.envpol.2020.115042.
6. Venter, Z.S.; Aunan, K.; Chowdhury, S.; Lelieveld, J. COVID-19 lockdowns cause global air pollution declines. *P. Natl. Acad. Sci.* **2020**, *117*, 18984–18990. doi:10.1073/pnas.2006853117.
7. Zhang, Z.; Arshad, A.; Zhang, C.; Hussain, S.; Li, W. Unprecedented Temporary Reduction in Global Air Pollution Associated with COVID-19 Forced Confinement: A Continental and City Scale Analysis. *Remote Sensing* **2020**, *12*. doi:10.3390/rs12152420.
8. Barré, J.; Petetin, H.; Colette, A.; Guevara, M.; Peuch, V.H.; Rouil, L.; Engelen, R.; Inness, A.; Flemming, J.; Pérez García-Pando, C.; Bowdalo, D.; Meleux, F.; Geels, C.; Christensen, J.H.; Gauss, M.; Benedictow, A.; Tsyro, S.; Friese, E.; Struzewska, J.; Kaminski, J.W.; Douros, J.; Timmermans, R.; Robertson, L.; Adani, M.; Jorba, O.; Joly, M.; Kouznetsov, R. Estimating lockdown-induced European NO_2 changes using satellite and surface observations and air quality models. *Atmos. Chem. Phys.* **2021**, *21*, 7373–7394. doi:10.5194/acp-21-7373-2021.
9. Bray, C.D.; Nahas, A.; Battye, W.H.; Aneja, V.P. Impact of lockdown during the COVID-19 outbreak on multi-scale air quality. *Atmos. Environ.* **2021**, *254*, 118386. doi:10.1016/j.atmosenv.2021.118386.
10. Dang, H.A.H.; Trinh, T.A. Does the COVID-19 lockdown improve global air quality? New cross-national evidence on its unintended consequences. *J. Environ. Econ. Manag.* **2021**, *105*, 102401. doi:10.1016/j.jeem.2020.102401.
11. Evangeliou, N.; Platt, S.M.; Eckhardt, S.; Lund Myhre, C.; Laj, P.; Alados-Arboledas, L.; Backman, J.; Brem, B.T.; Fiebig, M.; Flentje, H.; Marinoni, A.; Pandolfi, M.; Yus-Dìez, J.; Prats, N.; Putaud, J.P.; Sellegri, K.; Sorribas, M.; Eleftheriadis, K.; Vratolis, S.; Wiedensohler, A.; Stohl, A. Changes in black carbon emissions over Europe due to COVID-19 lockdowns. *Atmos. Chem. Phys.* **2021**, *21*, 2675–2692. doi:10.5194/acp-21-2675-2021.
12. Grange, S.K.; Lee, J.D.; Drysdale, W.S.; Lewis, A.C.; Hueglin, C.; Emmenegger, L.; Carslaw, D.C. COVID-19 lockdowns highlight a risk of increasing ozone pollution in European urban areas. *Atmos. Chem. Phys.* **2021**, *21*, 4169–4185. doi:10.5194/acp-21-4169-2021.
13. Guevara, M.; Jorba, O.; Soret, A.; Petetin, H.; Bowdalo, D.; Serradell, K.; Tena, C.; Denier van der Gon, H.; Kuenen, J.; Peuch, V.H.; Pérez García-Pando, C. Time-resolved emission reductions for atmospheric chemistry modelling in Europe during the COVID-19 lockdowns. *Atmos. Chem. Phys.* **2021**, *21*, 773–797. doi:10.5194/acp-21-773-2021.
14. Keller, C.A.; Evans, M.J.; Knowland, K.E.; Hasenkopf, C.A.; Modekurty, S.; Lucchesi, R.A.; Oda, T.; Franca, B.B.; Mandarino, F.C.; Díaz Suárez, M.V.; Ryan, R.G.; Fakes, L.H.; Pawson, S. Global impact of COVID-19 restrictions on the surface concentrations of nitrogen dioxide and ozone. *Atmos. Chem. Phys.* **2021**, *21*, 3555–3592. doi:10.5194/acp-21-3555-2021.
15. Solberg, S.; Walker, S.E.; Schneider, P.; Guerreiro, C. Quantifying the Impact of the Covid-19 Lockdown Measures on Nitrogen Dioxide Levels throughout Europe. *Atmosphere* **2021**, *12*. doi:10.3390/atmos12020131.
16. Piccoli, A.; Agresti, V.; Balzarini, A.; Bedogni, M.; Bonanno, R.; Collino, E.; Colzi, F.; Lacavalla, M.; Lanzani, G.; Pirovano, G.; Riva, F.; Riva, G.M.; Toppetti, A.M. Modeling the Effect of COVID-19 Lockdown on Mobility and NO2 Concentration in the Lombardy Region. *Atmosphere* **2020**, *11*. doi:10.3390/atmos11121319.
17. Collivignarelli, M.C.; Abbà, A.; Bertanza, G.; Pedrazzani, R.; Ricciardi, P.; Carnevale Miino, M. Lockdown for CoViD-2019 in Milan: What are the effects on air quality? *Sci. Total Environ.* **2020**, *732*, 139280. doi:10.1016/j.scitotenv.2020.139280.
18. Deserti, M.; Raffaelli, K.; Ramponi, L.; Carbonara, C.; Agostini, C.; Amorati, R.; Arvani, B.; Giovannini, G.; Maccaferri, S.; Poluzzi, V.; Stortini, M.; Trentini, A.; Tugnoli, S.; Vasconi, M. Report COVID-19 - Studio preliminare degli effetti delle misure COVID-19 sulle emissioni in atmosfera e sulla qualità dell'aria nel bacino padano - giugno 2020. Technical report, prepAIR project, 2020.
19. Deserti, M.; Raffaelli, K.; Ramponi, L.; Carbonara, C.; Agostini, C.; Amorati, R.; Arvani, B.; Giovannini, G.; Maccaferri, S.; Poluzzi, V.; Stortini, M.; Trentini, A.; Tugnoli, S.; Vasconi, M. Report 2 COVID-19 - Studio preliminare degli effetti delle misure COVID-19 sulle emissioni in atmosfera e sulla qualità dell'aria nel bacino padano - agosto 2020. Technical report, prepAIR project, 2020.
20. Rossi, R.; Ceccato, R.; Gastaldi, M. Effect of Road Traffic on Air Pollution. Experimental Evidence from COVID-19 Lockdown. *Sustainability* **2020**, *12*. doi:10.3390/su12218984.
21. Sicard, P.; De Marco, A.; Agathokleous, E.; Feng, Z.; Xu, X.; Paoletti, E.; Rodriguez, J.J.D.; Calatayud, V. Amplified ozone pollution in cities during the COVID-19 lockdown. *Sci. Total Environ.* **2020**, *735*, 139542. doi:10.1016/j.scitotenv.2020.139542.

22. Lonati, G.; Riva, F. Regional Scale Impact of the COVID-19 Lockdown on Air Quality: Gaseous Pollutants in the Po Valley, Northern Italy. *Atmosphere* **2021**, *12*. doi:10.3390/atmos12020264.
23. Granella, F.; Reis, L.A.; Bosetti, V.; Tavoni, M. COVID-19 lockdown only partially alleviates health impacts of air pollution in Northern Italy. *Environ. Res. Lett.* **2021**, *16*, 035012. doi:10.1088/1748-9326/abd3d2.
24. Cameletti, M. The Effect of Corona Virus Lockdown on Air Pollution: Evidence from the City of Brescia in Lombardia Region (Italy). *Atmos. Environ.* **2020**, *239*, 117794. doi:10.1016/j.atmosenv.2020.117794.
25. Putaud, J.P.; Pozzoli, L.; Pisoni, E.; Martins Dos Santos, S.; Lagler, F.; Lanzani, G.; Dal Santo, U.; Colette, A. Impacts of the COVID-19 lockdown on air pollution at regional and urban background sites in northern Italy. *Atmos. Chem. Phys. Discuss. [preprint]* **2020**, *2020*, 1–18. doi:10.5194/acp-2020-755.
26. Altuwayjiri, A.; Soleimanian, E.; Moroni, S.; Palomba, P.; Borgini, A.; De Marco, C.; Ruprecht, A.A.; Sioutas, C. The impact of stay-home policies during Coronavirus-19 pandemic on the chemical and toxicological characteristics of ambient PM2.5 in the metropolitan area of Milan, Italy. *Sci. Total Environ.* **2021**, *758*, 143582. doi:10.1016/j.scitotenv.2020.143582.
27. Lovarelli, D.; Conti, C.; Finzi, A.; Bacenetti, J.; Guarino, M. Describing the trend of ammonia, particulate matter and nitrogen oxides: The role of livestock activities in northern Italy during Covid-19 quarantine. *Environ. Res.* **2020**, *191*, 110048. doi:10.1016/j.envres.2020.110048.
28. Wang, Q.; Li, S. Nonlinear impact of COVID-19 on pollutions – Evidence from Wuhan, New York, Milan, Madrid, Bandra, London, Tokyo and Mexico City. *Sustain. Cities Soc.* **2021**, *65*, 102629. doi:10.1016/j.scs.2020.102629.
29. Rugani, B.; Caro, D. Impact of COVID-19 outbreak measures of lockdown on the Italian Carbon Footprint. *Sci. Total Environ.* **2020**, *737*, 139806. doi:10.1016/j.scitotenv.2020.139806.
30. Donzelli, G.; Cioni, L.; Cancellieri, M.; Llopis Morales, A.; Morales Suárez-Varela, M.M. The Effect of the Covid-19 Lockdown on Air Quality in Three Italian Medium-Sized Cities. *Atmosphere* **2020**, *11*. doi:10.3390/atmos11101118.
31. Toscano, D.; Murena, F. The Effect on Air Quality of Lockdown Directives to Prevent the Spread of SARS-CoV-2 Pandemic in Campania Region—Italy: Indications for a Sustainable Development. *Sustainability* **2020**, *12*. doi:10.3390/su12145558.
32. Vultaggio, M.; Varrica, D.; Alaimo, M.G. Impact on Air Quality of the COVID-19 Lockdown in the Urban Area of Palermo (Italy). *Int. J. Env. Res. Pub. He.* **2020**, *17*. doi:10.3390/ijerph17207375.
33. Bassani, C.; Vichi, F.; Esposito, G.; Montagnoli, M.; Giusto, M.; Ianniello, A. Nitrogen dioxide reductions from satellite and surface observations during COVID-19 mitigation in Rome (Italy). *Environ. Sci. Pollut. Res.* **2021**, *28*, 22981–23004. doi:10.1007/s11356-020-12141-9.
34. Gualtieri, G.; Brilli, L.; Carotenuto, F.; Vagnoli, C.; Zaldei, A.; Gioli, B. Quantifying road traffic impact on air quality in urban areas: A Covid19-induced lockdown analysis in Italy. *Environ. Pollut.* **2020**, *267*, 115682. doi:10.1016/j.envpol.2020.115682.
35. De Maria, L.; Caputi, A.; Tafuri, S.; Cannone, E.S.S.; Sponselli, S.; Delfino, M.C.; Pipoli, A.; Bruno, V.; Angiuli, L.; Mucci, N.; Ledda, C.; Vimercati, L. Health, Transport and the Environment: The Impacts of the COVID-19 Lockdown on Air Pollution. *Frontiers in Public Health* **2021**, *9*, 354. doi:10.3389/fpubh.2021.637540.
36. Malpede, M.; Percoco, M. Lockdown measures and air quality: evidence from Italian provinces. *Letters in Spatial and Resource Sciences* **2021**. doi:10.1007/s12076-021-00267-4.
37. Campanelli, M.; Iannarelli, A.M.; Mevi, G.; Casadio, S.; Diémoz, H.; Finardi, S.; Dinoi, A.; Castelli, E.; di Sarra, A.; Di Bernardino, A.; Casasanta, G.; Bassani, C.; Siani, A.M.; Cacciani, M.; Barnaba, F.; Di Liberto, L.; Argentini, S. A wide-ranging investigation of the COVID-19 lockdown effects on the atmospheric composition in various Italian urban sites (AER-LOCUS). *Urban Climate [accepted]* **2021**.
38. Sannino, A.; D'Emilio, M.; Castellano, P.; Amoruso, S.; Boselli, A. Analysis of Air Quality during the COVID-19 Pandemic Lockdown in Naples (Italy). *Aerosol Air Qual. Res.* **2021**, *21*, 200381. doi:10.4209/aaqr.2020.07.0381.
39. Chatterjee, A.; Mukherjee, S.; Dutta, M.; Ghosh, A.; Ghosh, S.K.; Roy, A. High rise in carbonaceous aerosols under very low anthropogenic emissions over eastern Himalaya, India: Impact of lockdown for COVID-19 outbreak. *Atmos. Environ.* **2021**, *244*, 117947. doi:10.1016/j.atmosenv.2020.117947.
40. Agnoletti, M.; Manganelli, S.; Piras, F. Covid-19 and rural landscape: The case of Italy. *Landscape Urban Plan.* **2020**, *204*, 103955. doi:10.1016/j.landurbplan.2020.103955.
41. Arduini, G.; Chemel, C.; Staquet, C. Local and non-local controls on a persistent cold-air pool in the Arve River Valley. *Q. J. Roy. Meteor. Soc.* **2020**, *146*, 2497–2521. doi:10.1002/qj.3776.
42. Herich, H.; Gianini, M.; Piot, C.; Močnik, G.; Jaffrezo, J.L.; Besombes, J.L.; Prévôt, A.; Hueglin, C. Overview of the impact of wood burning emissions on carbonaceous aerosols and PM in large parts of the Alpine region. *Atmos. Environ.* **2014**, *89*, 64–75. doi:10.1016/j.atmosenv.2014.02.008.
43. Bonvalot, L.; Tuna, T.; Fagault, Y.; Jaffrezo, J.L.; Jacob, V.; Chevrier, F.; Bard, E. Estimating contributions from biomass burning, fossil fuel combustion, and biogenic carbon to carbonaceous aerosols in the Valley of Chamonix: a dual approach based on radiocarbon and levoglucosan. *Atmos. Chem. Phys.* **2016**, *16*, 13753–13772. doi:10.5194/acp-16-13753-2016.
44. Diémoz, H.; Barnaba, F.; Magri, T.; Pession, G.; Dionisi, D.; Pittavino, S.; Tombolato, I.K.F.; Campanelli, M.; Della Ceca, L.S.; Hervo, M.; Di Liberto, L.; Ferrero, L.; Gobbi, G.P. Transport of Po Valley aerosol pollution to the northwestern Alps – Part 1: Phenomenology. *Atmos. Chem. Phys.* **2019**, *19*, 3065–3095. doi:10.5194/acp-19-3065-2019.

45. Diémoz, H.; Gobbi, G.P.; Magri, T.; Pession, G.; Pittavino, S.; Tombolato, I.K.F.; Campanelli, M.; Barnaba, F. Transport of Po Valley aerosol pollution to the northwestern Alps – Part 2: Long-term impact on air quality. *Atmos. Chem. Phys.* **2019**, *19*, 10129–10160. doi:10.5194/acp-19-10129-2019.
46. Fasano, G.; Diémoz, H.; Fountoulakis, I.; Cassardo, C.; Kudo, R.; Siani, A.M.; Ferrero, L. Vertical profile of the aerosol direct radiative effect in an Alpine valley, by the synergy of ground-based measurements and radiative transfer simulations. *B. Atmos. Sci. Tech. [under review]* **2021**.
47. Grappein, B.; Lasagna, M.; Capodaglio, P.; Caselle, C.; Luca, D.A.D. Hydrochemical and Isotopic Applications in the Western Aosta Valley (Italy) for Sustainable Groundwater Management. *Sustainability* **2021**, *13*. doi:10.3390/su13020487.
48. Campanelli, M.; Mascitelli, A.; Sanò, P.; Diémoz, H.; Estellés, V.; Federico, S.; Iannarelli, A.M.; Fratarcangeli, F.; Mazzoni, A.; Realini, E.; Crespi, M.; Bock, O.; Martínez-Lozano, J.A.; Dietrich, S. Precipitable water vapour content from ESR/SKYNET sun–sky radiometers: validation against GNSS/GPS and AERONET over three different sites in Europe. *Atmos. Meas. Tech.* **2018**, *11*, 81–94. doi:10.5194/amt-11-81-2018.
49. Patashnick, H.; Rupprecht, E.G. Continuous PM-10 Measurements Using the Tapered Element Oscillating Microbalance. *J. Air Waste Ma.* **1991**, *41*, 1079–1083. doi:10.1080/10473289.1991.10466903.
50. Green, D.C.; Fuller, G.W.; Baker, T. Development and validation of the volatile correction model for PM10 - An empirical method for adjusting TEOM measurements for their loss of volatile particulate matter. *Atmos. Environ.* **2009**, *43*, 2132–2141. doi:10.1016/j.atmosenv.2009.01.024.
51. Charron, A.; Harrison, R.M.; Moorcroft, S.; Booker, J. Quantitative interpretation of divergence between PM10 and PM2.5 mass measurement by TEOM and gravimetric (Partisol) instruments. *Atmos. Environ.* **2004**, *38*, 415–423. doi:10.1016/j.atmosenv.2003.09.072.
52. Cavalli, F.; Viana, M.; Yttri, K.E.; Genberg, J.; Putaud, J.P. Toward a standardised thermal-optical protocol for measuring atmospheric organic and elemental carbon: the EUSAAR protocol. *Atmos. Meas. Tech.* **2010**, *3*, 79–89. doi:10.5194/amt-3-79-2010.
53. Drinovec, L.; Močnik, G.; Zotter, P.; Prévôt, A.S.H.; Ruckstuhl, C.; Coz, E.; Rupakheti, M.; Sciare, J.; Müller, T.; Wiedensohler, A.; Hansen, A.D.A. The "dual-spot" Aethalometer: an improved measurement of aerosol black carbon with real-time loading compensation. *Atmos. Meas. Tech.* **2015**, *8*, 1965–1979. doi:10.5194/amt-8-1965-2015.
54. Diémoz, H.; Siani, A.M.; Redondas, A.; Savastiouk, V.; McElroy, C.T.; Navarro-Comas, M.; Hase, F. Improved retrieval of nitrogen dioxide (NO_2) column densities by means of MKIV Brewer spectrophotometers. *Atmos. Meas. Tech.* **2014**, *7*, 4009–4022. doi:10.5194/amt-7-4009-2014.
55. Diémoz, H.; Siani, A.M.; Casadio, S.; Iannarelli, A.M.; R., C.G.; Savastiouk, V.; Cede, A.; Tiefengraber, M.; Müller, M. Advanced NO_2 retrieval technique for the Brewer spectrophotometer applied to the 20-year record in Rome, Italy. *Earth Syst. Sci. Data [under review]* **2021**.
56. Diémoz, H.; Campanelli, M.; Estellés, V. One Year of Measurements with a POM-02 Sky Radiometer at an Alpine EuroSkyRad Station. *J. Meteorol. Soc. Jpn.* **2014**, *92A*, 1–16. doi:10.2151/jmsj.2014-A01.
57. Estellés, V.; Campanelli, M.; Smyth, T.J.; Utrillas, M.P.; Martínez-Lozano, J.A. Evaluation of the new ESR network software for the retrieval of direct sun products from CIMEL CE318 and PREDE POM01 sun-sky radiometers. *Atmos. Chem. Phys.* **2012**, *12*, 11619–11630. doi:10.5194/acp-12-11619-2012.
58. Kudo, R.; Diémoz, H.; Estellés, V.; Campanelli, M.; Momoi, M.; Marenco, F.; Ryder, C.L.; Ijima, O.; Uchiyama, A.; Nakashima, K.; Yamazaki, A.; Nagasawa, R.; Ohkawara, N.; Ishida, H. Optimal use of the Prede POM sky radiometer for aerosol, water vapor, and ozone retrievals. *Atmos. Meas. Tech.* **2021**, *14*, 3395–3426. doi:10.5194/amt-14-3395-2021.
59. Campanelli, M.; Nakajima, T.; Olivieri, B. Determination of the solar calibration constant for a sun-sky radiometer: proposal of an in-situ procedure. *Appl. Opt.* **2004**, *43*, 651–659. doi:10.1364/AO.43.000651.
60. Dionisi, D.; Barnaba, F.; Diémoz, H.; Di Liberto, L.; Gobbi, G.P. A multiwavelength numerical model in support of quantitative retrievals of aerosol properties from automated lidar ceilometers and test applications for AOT and PM_{10} estimation. *Atmos. Meas. Tech.* **2018**, *11*, 6013–6042. doi:10.5194/amt-11-6013-2018.
61. Fernald, F.G. Analysis of atmospheric lidar observations: some comments. *Appl. Opt.* **1984**, *23*, 652–653. doi:10.1364/AO.23.000652.
62. Klett, J.D. Lidar inversion with variable backscatter/extinction ratios. *Appl. Opt.* **1985**, *24*, 1638–1643. doi:10.1364/AO.24.001638.
63. Hervo, M.; Poltera, Y.; Haefele, A. An empirical method to correct for temperature-dependent variations in the overlap function of CHM15k ceilometers. *Atmos. Meas. Tech.* **2016**, *9*, 2947–2959. doi:10.5194/amt-9-2947-2016.
64. Wiegner, M.; Geiß, A. Aerosol profiling with the Jenoptik ceilometer CHM15kx. *Atmos. Meas. Tech.* **2012**, *5*, 1953–1964. doi:10.5194/amt-5-1953-2012.
65. Kroll, J.H.; Heald, C.L.; Cappa, C.D.; Farmer, D.K.; Fry, J.L.; Murphy, J.G.; Steiner, A.L. The complex chemical effects of COVID-19 shutdowns on air quality. *Nat. Chem.* **2020**, *12*, 777–779. doi:10.1038/s41557-020-0535-z.
66. Breiman, L. Random Forests. *Mach. Learn.* **2001**, *45*, 5–32. doi:10.1023/A:1010933404324.
67. Grange, S.K.; Carslaw, D.C.; Lewis, A.C.; Boleti, E.; Hueglin, C. Random forest meteorological normalisation models for Swiss PM_{10} trend analysis. *Atmos. Chem. Phys.* **2018**, *18*, 6223–6239. doi:10.5194/acp-18-6223-2018.
68. Grange, S.K.; Carslaw, D.C. Using meteorological normalisation to detect interventions in air quality time series. *Sci. Total Environ.* **2019**, *653*, 578–588. doi:10.1016/j.scitotenv.2018.10.344.
69. Petetin, H.; Bowdalo, D.; Soret, A.; Guevara, M.; Jorba, O.; Serradell, K.; Pérez García-Pando, C. Meteorology-normalized impact of the COVID-19 lockdown upon NO2 pollution in Spain. *Atmos. Chem. Phys.* **2020**, *20*, 11119–11141. doi:10.5194/acp-20-11119-2020.

70. Gariazzo, C.; Silibello, C.; Finardi, S.; Radice, P.; Piersanti, A.; Calori, G.; Cecinato, A.; Perrino, C.; Nussio, F.; Cagnoli, M.; Pelliccioni, A.; Gobbi, G.P.; Di Filippo, P. A gas/aerosol air pollutants study over the urban area of Rome using a comprehensive chemical transport model. *Atmos. Environ.* **2007**, *41*, 7286–7303. doi:10.1016/j.atmosenv.2007.05.018.
71. Silibello, C.; Calori, G.; Brusasca, G.; Giudici, A.; Angelino, E.; Fossati, G.; Peroni, E.; Buganza, E. Modelling of PM10 concentrations over Milano urban area using two aerosol modules. *Environ. Modell. Softw.* **2008**, *23*, 333–343. New Approaches to Urban Air Quality Modelling, doi:10.1016/j.envsoft.2007.04.002.
72. Cesaroni, G.; Badaloni, C.; Gariazzo, C.; Stafoggia, M.; Sozzi, R.; Davoli, M.; Forastiere, F. Long-Term Exposure to Urban Air Pollution and Mortality in a Cohort of More than a Million Adults in Rome. *Environ. Health Persp.* **2013**, *121*, 324–331. doi:10.1289/ehp.1205862.
73. Carter, W. Documentation of the SAPRC-99 Chemical Mechanism for VOC Reactivity Assessment. Final Report to California Air Resources Board, Contract 92-329 and 95-308, SAPRC. Technical report, University of California, Riverside, CA, 2000.
74. Binkowski, F., Science Algorithms of the EPA Models-3 Community Multiscale Air Quality (CMAQ) Modeling System; DW Byun, and JKS Ching (Eds), 1999; Vol. EPA/600/R-99/030, chapter The aerosol portion of Models-3 CMAQ.
75. EMEP/EEA. EEA Report No 13/2019 - EMEP/EEA air pollutant emission inventory guidebook 2019. Technical report, European Environment Agency, 2019. doi:0.2800/293657.
76. Mailler, S.; Menut, L.; Khvorostyanov, D.; Valari, M.; Couvidat, F.; Siour, G.; Turquety, S.; Briant, R.; Tuccella, P.; Bessagnet, B.; Colette, A.; Létinois, L.; Markakis, K.; Meleux, F. CHIMERE-2017: from urban to hemispheric chemistry-transport modeling. *Geosci. Model Dev.* **2017**, *10*, 2397–2423. doi:10.5194/gmd-10-2397-2017.
77. Geai, P. Méthode d'interpolation et de reconstitution tridimensionelle d'un champ de vent: le code d'analyse objective Minerve Report EDF/DER. Technical Report Report ARD-AID: E34-E11, Electricité de France, 1987.
78. Cox, R.M.; Sontowski, J.; Dougherty, C.M. An evaluation of three diagnostic wind models (CALMET, MCSCIPUF, and SWIFT) with wind data from the Dipole Pride 26 field experiments. *Meteorol. Appl.* **2005**, *12*, 329–341. doi:10.1017/S1350482705001908.
79. Sokhi, R.; Kitwiroon, N.; Luhana, L. FUMAPEX Datasets of Urban Air Pollution Models and Meteorological Preprocessors. In *Fumapex Report D*; 2003; Vol. 2, pp. 1–D2.
80. Paatero, P.; Tapper, U. Positive matrix factorization: A non-negative factor model with optimal utilization of error estimates of data values. *Environmetrics* **1994**, *5*, 111–126. doi:10.1002/env.3170050203.
81. Paatero, P. Least squares formulation of robust non-negative factor analysis. *Chemometr. Intell. Lab.* **1997**, *37*, 23–35. doi:10.1016/S0169-7439(96)00044-5.
82. Norris, G.; Duvall, R. *EPA Positive Matrix Factorization (PMF) 5.0 – Fundamentals and User Guide*. U.S. Environmental Protection Agency, 2014.
83. Fuller, K.A.; Malm, W.C.; Kreidenweis, S.M. Effects of mixing on extinction by carbonaceous particles. *J. Geophys. Res.* **1999**, *104*, 15941–15954. doi:10.1029/1998JD100069.
84. Bond, T.C.; Bergstrom, R.W. Light Absorption by Carbonaceous Particles: An Investigative Review. *Aerosol Sci. Tech.* **2006**, *40*, 27–67. doi:10.1080/02786820500421521.
85. Hitzenberger, R.; Petzold, A.; Bauer, H.; Ctyroky, P.; Pouresmaeil, P.; Laskus, L.; Puxbaum, H. Intercomparison of Thermal and Optical Measurement Methods for Elemental Carbon and Black Carbon at an Urban Location. *Envir. Sci. Tech.* **2006**, *40*, 6377–6383. doi:10.1021/es051228v.
86. Sandradewi, J.; Prévôt, A.S.H.; Szidat, S.; Perron, N.; Alfarra, M.R.; Lanz, V.A.; Weingartner, E.; Baltensperger, U. Using Aerosol Light Absorption Measurements for the Quantitative Determination of Wood Burning and Traffic Emission Contributions to Particulate Matter. *Envir. Sci. Tech.* **2008**, *42*, 3316–3323. doi:10.1021/es702253m.
87. Titos, G.; del Águila, A.; Cazorla, A.; Lyamani, H.; Casquero-Vera, J.; Colombi, C.; Cuccia, E.; Gianelle, V.; Močnik, G.; Alastuey, A.; Olmo, F.; Alados-Arboledas, L. Spatial and temporal variability of carbonaceous aerosols: Assessing the impact of biomass burning in the urban environment. *Sci. Total Environ.* **2017**, *578*, 613–625. doi:10.1016/j.scitotenv.2016.11.007.
88. Cristofanelli, P.; Arduni, J.; Serva, F.; Calzolari, F.; Bonasoni, P.; Busetto, M.; Maione, M.; Sprenger, M.; Trisolino, P.; Putero, D. Negative ozone anomalies at a high mountain site in northern Italy during 2020: a possible role of COVID-19 lockdowns? *Environ. Res. Lett.* **2021**. doi:10.1088/1748-9326/ac0b6a.
89. Nicolás, J.; Yubero, E.; Galindo, N.; Giménez, J.; Castañer, R.; Carratalá, A.; Crespo, J.; Pastor, C. Characterization of events by aerosol mass size distributions. *J. Environ. Monit.* **2009**, *11*, 394–399. doi:10.1039/B813042F.
90. Gobbi, G.; Barnaba, F. Di Liberto, L.; Bolignano, A.; Lucarelli, F.; Nava, S.; Perrino, C.; Pietrodangelo, A.; Basart, S.; Costabile, F.; Dionisi, D.; Rizza, U.; Canepari, S.; Sozzi, R.; Morelli, M.; Manigrasso, M.; Drewnick, F.; Struckmeier, C.; Poenitz, K.; Wille, H. An inclusive view of Saharan dust advections to Italy and the Central Mediterranean. *Atmos. Environ.* **2019**, *201*, 242 – 256. doi:10.1016/j.atmosenv.2019.01.002.
91. Huang, X.; Ding, A.; Gao, J.; Zheng, B.; Zhou, D.; Qi, X.; Tang, R.; Wang, J.; Ren, C.; Nie, W.; Chi, X.; Xu, Z.; Chen, L.; Li, Y.; Che, F.; Pang, N.; Wang, H.; Tong, D.; Qin, W.; Cheng, W.; Liu, W.; Fu, Q.; Liu, B.; Chai, F.; Davis, S.J.; Zhang, Q.; He, K. Enhanced secondary pollution offset reduction of primary emissions during COVID-19 lockdown in China. *Natl. Sci. Rev.* **2020**, *8*. nwaa137, doi:10.1093/nsr/nwaa137.